

PRIIT PRIIMÄGI

Development and optimization of
3D-microbatteries



PRIIT PRIIMÄGI

Development and optimization of
3D-microbatteries



Institute of Technology, Faculty of Science and Technology, University of Tartu, Estonia

Dissertation was accepted for the commencement of the degree of Doctor of Philosophy in Materials Science on October 18, 2018 by the Council of the Institute of Technology, University of Tartu.

Supervisors: Vahur Zadin, PhD, Institute of Technology
Faculty of Science and Technology
University of Tartu, Estonia

Heiki Kasemägi, PhD, Institute of Technology
Faculty of Science and Technology
University of Tartu, Estonia

External Supervisor: Prof. Daniel Brandell, PhD, Department of Chemistry,
Ångström
Uppsala University, Sweden

Opponent: Prof. Senentxu Lanceros-Mendez, PhD
BCMaterials, Basque Center for Materials, Applications
and Nanostructures, Spain

The public defense will take place on December 11, 2018 at Auditorium 121 in Nooruse 1, Tartu, Estonia

The publication of this dissertation was financed by the Institute of Technology, Faculty of Science and Technology, University of Tartu.



European Union
European Regional
Development Fund



Investing
in your future

ISSN 2228-0928
ISBN 978-9949-77-909-3 (print)
ISBN 978-9949-77-910-9 (pdf)

Copyright: Priit Priimägi, 2018

University of Tartu Press
www.tyk.ee

*The Stone Age did not end because humans ran out of stones.
It ended because it was time for a re-think about how we live.*
-William McDonough

CONTENTS

ABSTRACT	9
LIST OF PUBLICATIONS	11
ABBREVIATIONS AND SYMBOLS	12
1 INTRODUCTION	14
1.1 A brief history of Li-ion batteries	15
1.2 Working principles of Li-ion batteries	16
1.3 Common limitations of the Li-ion cells	17
1.4 3D microbatteries	18
1.5 3D microbattery design	20
1.6 Computer simulations	22
1.7 Scope of the thesis	23
2 METHODOLOGY	25
2.1 Finite element method	25
2.2 Electrochemical model of Li-ion batteries	26
2.2.1 Li-ion transport in the electrolyte	28
2.2.2 Electric potential in the electrolyte	29
2.2.3 Li-ion transport in the electrode	30
2.2.4 Potential in the electrode	31
2.2.5 Electrochemical kinetics	31
2.3 Thermal model of Li-ion batteries	32
2.4 Simulated 3D-MB architectures and materials	34
3 RESULTS AND DISCUSSION	37
3.1 General charge-discharge characteristics of the 3D-MB	37
3.2 Benchmarking different architectures for 3D-MBs	38
3.3 Optimization of the electrode dimensions in concentric architecture	40
3.3.1 Variation of pillar heights	40
3.3.2 Variation of interpillar distance	43
3.4 Parametric studies of the aperiodic MB architecture	45
3.4.1 Charge characteristics	45
3.4.2 Current density in the carbon and concentration gradient in the electrolyte	46
3.4.3 LiFePO ₄ delithiation and coating homogeneity	48
3.4.4 LiFePO ₄ coating thickness	49
3.4.5 Carbon foam macropore size	50
3.5 Thermal effects in different microbattery architectures	51
3.6 Designing 3D microbatteries	55
3.6.1 Polymer electrolyte vs. liquid electrolyte	55
3.6.2 Electrode material rearrangement in the concentric architecture	56
3.6.3 Comparison of 3D MB architectures	58

4 CONCLUSION AND OUTLOOK	60
5 SUMMARY IN ESTONIAN	63
6 ACKNOWLEDGMENTS	65
7 APPENDIX	66
8 REFERENCES	67
PUBLICATIONS	73
CURRICULUM VITAE	115
ELULOOKIRJELDUS	116

ABSTRACT

Electronics and portable devices are under continual developing and upgrading. Therefore, smaller and more powerful technology requires compatible energy source and storing systems. In that sense much effort is devoted to the development of batteries with smaller dimensions and higher energy capabilities where one area of research is focused on designing micro scale batteries to supply very small appliances with energy. Here 3-dimensional microbattery concept is proposed to achieve appropriate higher energy and power density than conventional planar battery cell technology should provide.

In this thesis, four different 3D Li-ion microbattery concepts are computationally developed, modelled and optimized using finite element method. The studies aimed at enriching the fundamental understanding of the mass transport occurring in these complex architectures and to find optimal electrode geometrical configurations to achieve higher cell capacity, smoother lithiation/delithiation and homogeneous electrochemical activity over the electrode surfaces via parametric simulations.

The electrochemical-thermal coupled simulations highlight the chemically active regions in these different microbattery architectures and points out possible heat sources and mass transport bottlenecks. It was found that concentric architecture has the highest capacity 93 mAh/g while interdigitated and trench architecture exposed 86 and 80 mAh/g respectively. Also somewhat higher temperature development was observed in the trench system. In further investigation of pillared electrode architecture showed that deeper delithiation and higher active material utilization was achieved in the LiCoO_2 positive electrode when shorter pillars are used. Higher pillars on the other hand presented somewhat higher overall energy capacity with the cost of underutilized material regions. Therefore, optimal pillar height should be around 70 μm with the inter-pillar distance of 12 μm for the concentric architecture.

Additionally, carbon foam type composite electrode was successfully calibrated against the experimental results. Parametric simulations revealed that smaller macropores and thicker coatings provides higher capacity per electrode footprint area and no other limiting factors was observed. The electrochemical reactions prefer particles near to the carbon foam structure and delithiation is very homogeneous.

In conclusion, electrochemical simulations of Li-ion batteries can be very useful tool for developing and designing the Li-ion battery architecture. It allows easily change material parameters and geometrical dimensions of the electrode and electrolyte to find optimal cell configuration and best cell performance. Although, it should be mentioned that it is relatively difficult to experimentally produce these theoretically well performing 3D-electrodes and complex cell architectures and therefore synthesis and assembling methods and fabrication techniques should be further developed.

Keywords: Li-ion microbattery, 3-dimensional, electrochemical-thermal modeling, finite element method, parametric variation, simulation calibration, optimization, foam-type electrode, LiCoO_2 , LiFePO_4 , graphite, polymer electrolyte, liquid electrolyte.

LIST OF PUBLICATIONS

The current thesis is based on the following original publications:

- I P. Priimägi, D. Brandell, S. Srivastav, A. Aabloo, H. Kasemägi, and V. Zadin, “Optimizing the design of 3D-pillar microbatteries using finite element modelling,” *Electrochim. Acta*, vol. 209, pp. 138–148, 2016.
- II P. Priimägi, H. Kasemägi, A. Aabloo, D. Brandell, and V. Zadin, “Thermal Simulations of Polymer Electrolyte 3D Li-Microbatteries,” *Electrochim. Acta*, vol. 244, pp. 129–138, 2017.
- III P. Priimägi, H. D. Asfaw, S. Srivastav, H. Kasemägi, A. Aabloo, D. Brandell, and V. Zadin, “Modeling 3D-microbatteries based on carbon foams,” *Electrochim. Acta*, vol. 281, pp. 665–675, 2018.

The publications that the theses based on, are a result of a collective effort from all of the co-authors. The author contribution to the articles I-III were the research in the field, boundary conditions and material parameters implementation, carrying out the simulations, interpreting the results and writing.

Other publications to which the author has contributed but which are not included in the present theses:

- IV D. Brandell, P. Priimägi, H. Kasemägi, and A. Aabloo, “Branched polyethylene/poly (ethylene oxide) as a host matrix for Li-ion battery electrolytes: A molecular dynamics study,” *Electrochim. Acta*, vol. 57, pp. 228–236, 2011.
- V A-L Peikolainen, P. Priimägi, H. Kasemägi, V. Zadin, D. Brandell, M. Uibu, and A. Aabloo (2017) “Tuning of carbon xerogel for Na-ion battery anode,” In: Program Guide and Abstracts (506) .Solid State Ionics- 21st International Conference, Padua- Italy, June 18–23, 2017.

ABBREVIATIONS AND SYMBOLS

MEMS	Microelectromechanical systems
3D-MBs	3 dimensional microbatteries
DFT	Density Functional Theory
MD	Molecular Dynamics
FEM	Finite Element Method
FEA	Finite Element Analysis
PDEs	Partial differential equations
VTF	Vogel-Tamman-Fulcher
LCO	LiCoO ₂
LFP	LiFePO ₄
PEO	Poly(ethylene oxide)
EC	Ethylene carbonate
DEC	Dimethyl carbonate
SOC	State of charge
A	Concentration dependent pre-exponential factor ($\text{K}^{0.5} \text{m}^2/\text{s}$)
a	Current collector contact surface area (m^2)
a_s	Area per unit volume of the intercalation particles ($1/\text{m}$)
c_i	Concentration of specie i (mol/m^3)
c_s	Concentration of the intercalating species (mol/m^3)
$c_{s,max}$	Maximum concentration in solid (mol/m^3)
c_{tot}	Sum of the concentrations
C_p	Heat capacity ($\text{J}/(\text{kg}\cdot\text{K})$)
$D_{0,a}, D_{0,c}$	Anodic and cathodic initial solid state diffusion (m^2/s)
D_{ij}	Diffusion coefficient for the interaction between the two species i and j (m^2/s)
D_s	Diffusion coefficient in the solid phase (m^2/s)
D^{eff}	Effective diffusion coefficient in the solid phase (m^2/s)
D_e	Diffusion coefficient in the electrolyte (m^2/s)
d	Interpillar distance (m)
$d_{electrolyte}$	Thickness of the electrolyte (m)
E_a	Electrolyte pseudo-activation energy (eV)
F	Faraday's constant 96485 (C/mol)
f_{+-}	Average molar activity coefficient (mol/m^3)
h	Pillar height (m)
h_{neg}	Base layer thickness of negative electrode (m)
H_{pos}	Base layer thickness of positive electrode (m)
I	Current (A)
i	Applied current density (A/m^2)
i_s	current density in the electrode (A/m^2)
i_0	Exchange current density (A/m^2)
J	Intercalation current density (A/m^2)

j_{in}	Flux into the particles (mol/m ² s)
j^{Li}	Volumetric rate of reaction at the particle surface (mol/m ³ s)
k_B	Boltzmann constant 8.617·10 ⁻⁵ (eV/K)
$k_{0,a}, k_{0,c}$	Anodic and cathodic initial kinetic rate (m/s)
k_a, k_c	Anodic and cathodic kinetic rate constants (m/s)
k	Thermal conductivity (W/(m·K))
N_+	Molar flux of Li-ions (mol/m ² s)
Q	Total heat generation (W/m ³)
Q_{rev}	Reversible heating (W/m ³)
Q_{JH}	Joule heating (W/m ³)
R	Universal gas constant (8.314 J/(mol K))
R_i	Reaction rate of the cation or anion per unit volume (mol/m ³ s)
R_{cc}	Resistance of current collector (Ω)
r	Radius of the pillar (m)
r_s	radius of the spherical active material particle (m)
r_{cc}	Radius of the current collector (m)
ΔS	Entropy change (J/K)
T	Temperature (K)
T_0	Ideal glass transition temperature (K)
T_g	Electrolyte glass transition temperature (K)
t	Time (s)
t_+^0	Electrolyte transference number
U_{eq}	Thermodynamic equilibrium potential in the solid phase (V)
v_0	Convection of the electrolyte (m/s)
v_i	Velocity of specie I (m/s)
z_+, z_-	Charge of the positive and negative specie

Greeks

α_a and α_c	Anodic and cathodic transfer coefficients
γ	Bruggeman's constant (1.5)
ε_l	Electrolyte volume fraction
ε_s	Solid phase volume fraction
η	Activation overpotential (V)
Φ	Potential of the electrode (V)
κ^{eff}	Effective ionic conductivity of the electrolyte (S/m)
κ_e	Ionic conductivity of the electrolyte (S/m)
$\Delta\mu$	Gradient of the electrochemical potential (V)
ρ	Material density (kg/m ³)
σ_s	Electronic conductivity of the electrode (S/m)
σ_s^{eff}	Effective electronic conductivity in the solid (S/m)
φ_s	Potential in solid phase (V)
φ_l	Potential in electrolyte (V)

1 INTRODUCTION

Each generation is opposed with new opportunities and challenges. According to the International Energy Agency the global energy consumption was about 109613 TWh in 2014 and this ever increasing world energy demand due to the growing population has to be satisfied [1]. To date fossil fuels such as oil, coal and natural gas has undoubtedly been the most utilized energy sources, which together account for around 80% of the overall energy consumption [1]. Moreover, long-term energy production using fossil fuels has caused serious emission problems for the environment and pollution that threatens human health especially in the big cities. This has led to a significant progress by the development of alternative energy sources to prevent these issues for future generations. Therefore, considerable efforts are now focused to develop cleaner and reliable technology based energy sources such as nuclear, solar, hydro and other renewable bioenergy applications to meet the demand and possibly to start replacing the major sources. Although, most of the renewable energy sources are strongly weather and location dependent and therefore harvested energy should be accumulated when needed and transported using power grids.

Also, the air pollution in metropolises can be reduced using zero emission transport technology for example electrical public transportation and electrical or hybrid vehicles. Unfortunately, energy storage system for such electric transportation is unsuitable for wide commercial usage and is very expensive. Therefore, the key for successful breakthrough lies in the development of energy storage devices which are cheap, reliable and have high energy and power density. This in turn is a fascinating scientific challenge, in which material science and chemistry will play significant role.

The current suitable and leading energy storage technology is undoubtedly the rechargeable electrochemical battery. Battery is a device which consists one or more electrochemical cells and converts the stored chemical energy into useful electrical energy. Every individual electrochemical cell comprises of two electrodes an anode, a cathode and an electrolyte between electrodes. These materials provide energy conversion through reduction and oxidation reactions in the electrodes on account of which electrons flow through an outer circuit. The desired spontaneous process is a discharge cycle where electrons move through the appliance from the negative electrode to the positive electrode and therefore useful work is performed.

Generally there is a wide range of possible battery technologies, mainly with different cell chemistries. These cells are divided into two main categories: a) primary batteries – which only allow a single discharge process b) secondary batteries – however, enables reversible electrochemical reaction processes which in turn allows recharge the battery by applying the external voltage across the electrode terminals. In another words charger uses extra energy and pushes electrons from the positive electrode back to the negative electrode till the certain voltage level of the battery is reached. One of the primary battery

type is alkaline batteries where alkaline electrolyte (potassium hydroxide) and reaction between zinc and manganese dioxide (Zn/MnO_2) occurs [2,3]. These low self-discharge batteries are useful to power small household appliances where both long periods of energy storage and low current are required. In contrast secondary batteries are practically more economical because of the numerous cycling ability and are therefore used in the portable electronic devices, hand-held power tools and electrical vehicles. Therefore, several different material combinations are introduced where the most popular secondary battery technologies are lead-acid (Pb-acid), nickel-cadmium (NiCd), nickel-metal hydride (NiMH) and Lithium-ion batteries (Li-ion) [4]. However, Lithium metal based technology is considered to be the youngest compare to the other battery technologies, the popularity of usage in a wide range of applications increases. While the future of this technology looks bright, there is ongoing investigation and extensive development in a field of material science to find new and amended materials for reducing the production cost and improving the battery performance and safety. This current research is one of the example, which focuses on designing and optimizing new 3-dimensional electrode architectures for the Lithium-ion microbatteries and trying to investigate the key properties of these electrochemical cells.

1.1 A brief history of Li-ion batteries

The first electrochemical cell that produces electrical current was introduced by Alessandro Volta in 1800, where discs of zinc and copper with piece of cardboard are soaked into brine [3]. Later in 1880s, first lead-acid rechargeable battery was introduced by the French physicist Gaston Plante [3]. This invention was big step in the field of battery development and hereby commercialization of the secondary battery was initiated. In contrast Lithium metal was introduced in battery technology already back in 1958 by the work of Harris [5]. The motivation behind the idea of using active Lithium metal as an electrode in the batteries was due to the lightest weight of the metal (0.53 g/cm^3) and Lithium is the most electropositive (-3.04V vs. standard hydrogen electrode) which in turn provides utmost energy density of all metals [6]. Lithium battery technology was therefore very promising and continuing researches led to the development of the primary Lithium cell during the 1970s. Still, secondary Lithium batteries was introduced about 10 years later 1980s. This type of electrochemical cells had its own advantages and disadvantages, thus most of the work focuses on finding the suitable electrode materials, which can insert and remove Lithium-ions in the certain voltage range without a large change of the host lattice dimensions [5]. Eventually, in 1991 first commercial rechargeable Lithium-ion cell was presented by Sony [6]. This cell bases on graphite negative electrode and LiCoO_2 positive electrode, with an high operating voltage window (exceeding 3.6 V) [6,7]. This was a scientific breakthrough which initiates the extra amount of work in the battery development field where

design of the battery and manufacturing process development became under radar. Since then the material science on all aspects of the cell chemistry increases extraordinary popularity. Surely, various Lithium battery chemistries can be applied under numerous combinations of anodes, cathodes and electrolyte materials. Therefore, different approaches are nowadays divided into research topics i.e. “Lithium-ion”, “Lithium-ion-polymer”, “solid polymer electrolytes”, “liquid electrolytes” and into all types of usable electrodes. Besides, Li-ion battery can consist of different type of electrodes – “thin film”, “thick film” or “3 dimensional electrodes” where latter is also studied furthermore in this research.

1.2 Working principles of Li-ion batteries

Primarily Li-ion cells, as any other batteries, consist of a two electrodes and an electrolyte. Main function of the electrodes is to store Li-ions and are named by the characteristic electrochemical reactions as the positive electrode and the negative electrode. The electrolyte is between the electrodes with a purpose of transporting media for the Li-ions to shuttle from one electrode to another. Schematic of the typical Li-ion battery with Lithium cobalt oxide (LiCoO_2) as the positive electrode and graphite (LiC_6) as the negative electrode is represented in the Figure 1. The main working conception of the Li-ion battery is that electrons should travel only through the external circuit and Li-ions through the electrolyte, which defines first critical properties of the electrolyte. Whether the electrolyte is liquid or solid, it has to provide highest ionic conductivity and near to zero electronic conductivity.

Under discharge state, all the Li-ions are situated in the positive electrode and opposing negative electrode have empty sites for ions. During charging, electrons are externally detracted from the positive electrode and pushed into the negative electrode. With each electron equal amount of Li-ions are released from the LiCoO_2 host structure into the electrolyte and incoming electrons on the negative electrode attracts the Li-ions from the electrolyte. Therefore Li-ions are inserted into the graphite structure till the LiCoO_2 is reached the depleted state and certain cell voltage is developed. During discharge the processes are reversed and useful current is created due to the externally moving electrons. Herewith, depending on the discharge or charge processes, the graphite as a negative electrode stands as an anode or a cathode respectively. Common conception is that when phrases anode and cathode are used then, implicitly discharge process is under discussion.

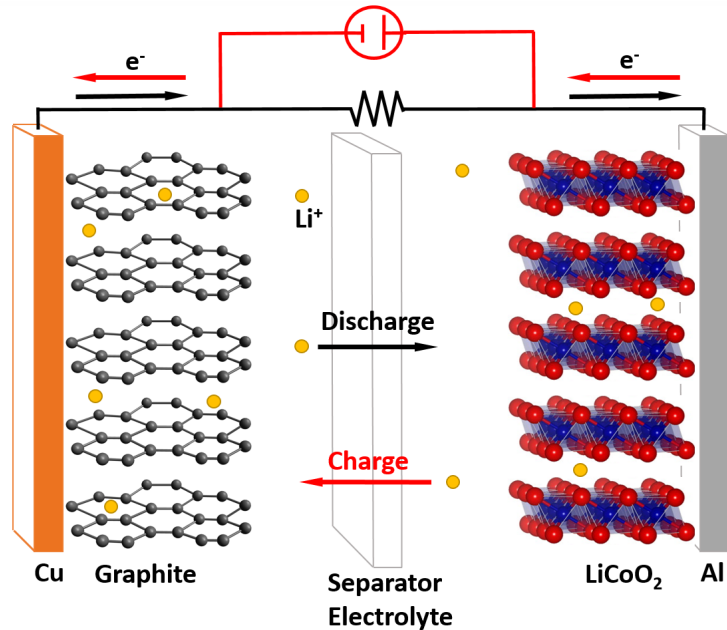


Figure 1. Schematic representation of the Li-ion cell.

1.3 Common limitations of the Li-ion cells

However, currently Li-ion cell provides the highest energy density (J/m^3) in the field of battery technology, but in the same time power density (W/m^3) is limited [5]. In vice versa, when battery can deliver high power then usually energy density as cell capacity (mAh/g) is not high enough. This behavior depends mostly on the coating thickness of the working electrode material on the current collector. Therefore, thin film batteries which are composed of parallel thin layers of coated active materials, have large electrode surface area for supporting sustainable high current, but only for a short period of time and thus will suffer from limited energy densities. Thick film batteries, on the contrary, where increased thickness of the active material layer leads to the improved capacity, but related longer ionic diffusion pathway renders a decrease in the current and power density of the cell [8]. Thus, these different approached can be used to assure the consumer needs respectively.

Another important aspect in the cell construction is to choose right material for the electrolyte. While most of the Li-ion batteries have lithiated graphite as a negative electrode, then electrochemical intercalation of lithium ions into graphite occurs around 0.2 V. Therefore electrolyte in these batteries should be electrochemically stable under this potential level, otherwise unwanted reactions will occur and decomposition of mixture of compounds passivates

further the electrochemical reactions on the electrode surface. Typically most important characterization of the electrolytes are the ionic conductivity, salt diffusion coefficient and cation transference number [9]. It should be noticed that these properties should be measured as a function of concentration and temperature. Additional character of the electrolyte is a melting or crystallization point where the electrolyte morphology changes. When cell is assembled using for example solid or polymer electrolyte then one should be mechanically protect the cell for short circuiting the electrodes. Cells with liquid electrolytes on the other hand, typically with improved ionic conductivity, should therefore consist separator to prevent cell short circuit issues. These aspects plays very important role when designing cell architectures.

One of the challenge in the battery industry is to produce safe and reliable cells. When Li-metal based electrodes are used in the battery to enhance the energy density of the cell, then unfortunately, formation of the lithium dendrites occurs. Therefore, these inner conductive pathways inflict electrodes short circuits, which significantly decreases lifetime of these type of cells and makes it unsafe. While inner shorts provoke high material temperatures then flammable electrolytes and Li-metal contact with humidity causes environmental and human health concerns. In that sense approaches for safety improvement are interest of the research where some of the strategies can be: utilizing stable solid polymer electrolytes [10–12] and multilayer separators [13], using electrolytes with additives [14–16] and redox shuttles [3,5,13] to enhance the thermal stability and protect battery from overcharge respectively.

Besides the development of the Li-ion battery safeness, the cell performance is expected to improve with implementing new nanomaterials and novel architectures thru several key ways:

1. Shorter diffusion pathways – thinner electrolyte layers and electrode materials with smaller particle sizes to reduce the Li-ion transportation time from particle core to surface.
2. Higher surface are of the electrodes – allows to use higher charge and discharge rates and overall power density increases by using novel 3D electrode designs.
3. Decreasing mechanical stresses in the electrode during Li-ions insertion and detraction by using additives and innovative nanomaterials which in turn improve cell life time and power density.
4. Using current collectors to improve electrical conductivity of the electrode material and additionally provide mechanical support for the complex electrode structure.

1.4 3D microbatteries

During last decade, electronic industry has rapidly developed novel and smaller scale devices in the fields of micro sensors, medical implants and other self-powered microelectromechanical systems (MEMS) [17]. Such small size

devices integrates components as sensors, processor for signal processing, electronic circuit and power source into complete package with a volume of around 1–10 mm³ [18]. Herewith, batteries with a small scale and suitable discharge rates are preferred, which in turn creates a demand for research on reliable Li-ion microbatteries.

Commercialized battery technology, where 2D thin-film approach is used, provide high current rates but suffer from limited energy densities. Therefore, capacity increase is mostly obtained by rolling up the film with a high electrode surface area. Unfortunately, this technique is not suitable for microbatteries because of the possible cell inner short circuits due to the material mechanical failure during the operation. On the other hand, using thick-film electrodes in order to store more energy is also not viable technique because thicker coating reduces power density by increasing resistivity and also mechanical integrity of the electrode material decreases. In general, 2D planar cell battery design on a small footprint area, results in a tradeoff between energy density and power density, but is not sufficient energy storage for MEMS [13]. This problem can be solved when third dimension of the electrode is taken into account as illustrated in Figure 2. Thereby, design of the 3 dimensional (3D) electrodes allows storing increased amount of active material into the heights thru certain manner to provide appropriate energy and power density within a given footprint area [19,20]. Therefore, this approach offers: 1) large electrode surface area 2) increased electrode mass loading and 3) short ion transport distances in the material for minimizing power losses [21]. Naturally, the improved inner electrode electrolyte surface area provides lower local current densities which in turn allows to apply higher current on current collectors and therefore higher power is achieved on the same footprint area. When 3D architecture escalates the electrode area 10 times per footprint area then fundamentally it should respectively support order of magnitude higher current than 2D cells [22,23]. In this context, capacity per footprint area (mAh/cm²) becomes main unit when comparing microbatteries. Herewith, when typical commercial 2D thin-film cells gives 0.5 mAh/cm² then capacity of this 3D microbattery (3D-MB) using novel 3D electrode technology should approach around 10 mAh/cm² [24].

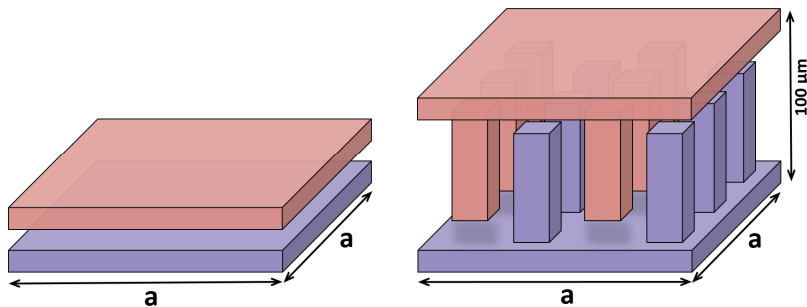


Figure 2. Schematic illustrations of conventional 2D film battery and 3D-MB concept.

1.5 3D microbattery design

The required combination of high power and energy density of the battery can be achieved thru 3D microbattery concept that provides increased internal surface area and mass loading of the active material under small footprint area [25]. To date, numerous 3D architectures of such current collectors and electrodes have been proposed as illustrated in Figure 3 [19]. One of the most investigated 3D geometry (Figure 3a) is interdigitated architecture, where both electrodes comprises a nanosized pillars or rods which are stacked in rows of intermittent cathodes and anodes. This configuration was introduced by Hart et al. [26] in 2003 and further experimental works are carried out by many others [27–30]. The key feature for this architecture is that pillars need to be in a periodic arrays, where one variation is to use plates instead of pillars, to increase the electrode area, called trench architecture (Figure 3b). This is technically similar approach when using 2D planar electrodes in a parallel connection. Trench design has been investigated by Notten et al. [16,31–33] and furthermore, Zadin et al. [34,35] studied the performance of this geometry using finite element methodology (FEM). Another 3D architecture named concentric (Figure 3c) utilized a rod array of current collectors which are coated with electrode material and is then coated with thin layer of electrolyte. At last, the rest of the volume is filled by the opposite electrode material and continuous phase is achieved. A primitive design of such geometry was introduced and successfully implemented in 2005 by Nathan and Golodnitsky group [15,36,37]. In contrast to the previous periodic architectures the foam type aperiodic geometry (Figure 3d) based on highly porous aerogel or carbon foam electrode with an extremely large specific surface area has been proposed [38–40]. Nevertheless, the foam design has its own benefits, the great efforts are still needed to develop an effective synthesise and fabrication processes.

From the previous list of proposed 3D Li-ion MB architectures, perhaps the greatest concern is the full cell implementation achieving durable mechanical properties and high cathode packing density with no voids in the materials. Yet, 3D Li-ion MBs are in the developing stage and most of the research exhibits half-cell systems with one functioning 3D electrode, still some have demonstrated full working cells. The first working 3D rechargeable Li-ion microbattery has developed in 2005 by Nathan et al. [36]. This plate with microchannels as sandwich-like structure of conformal thin-film electrodes, electrolyte and current collectors has order of magnitude higher surface area and runs for 200 cycles whereby providing capacity of 2 mAh/cm². On the other hand Kotobuki and co-workers [10,41], Min et al. [42] and Pikul et al. [29] have developed 3D-MBs applying different synthesise techniques but unfortunately these cells showed either very low capacity or short-circuited after couple of cycles. In 2013, Sun et al. printed high aspect ratio multilayer electrodes successfully in interdigitated architectures and measured capacity of 1.6 mAh/cm² using Li₄Ti₅O₁₂ and LiFePO₄ electrodes [28]. Group in Sweden, Brandell and Edström et al. have reported several 3D-MB fabrication methods and cell

designing approaches with various electrode and electrolyte materials exceeding reversible capacities in range of $(0.03 - 3.5 \text{ mAh/cm}^2)$ [43–46]. Recently, Li-ion half-cell using aperiodic design was introduced by Asfaw et al. where they measured footprint area capacity 1.72 mAh/cm^2 of novel 3D composite cathode fabricated from LiFePO_4 nanoparticles deposited conformably on a high porous carbon foam [47].

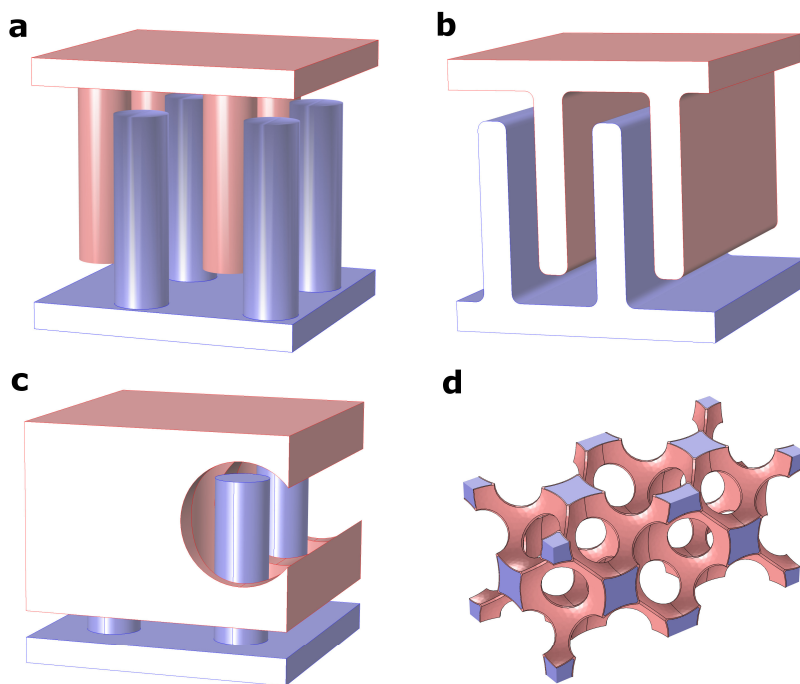


Figure 3. Proposed 3D architectures for microbatteries. a) Interdigitated – array of pillars; b) Trench – periodical plates; c) Concentric – pillared electrode is coated with electrolyte and filled up with opposite electrode material; d) Aperiodic structure – foam type electrode is coated with electrolyte and filled or coated with opposite electrode.

So far several works have proved that 3D-MBs are promising candidates for energy storing technology for MEMS. Moreover, battery capacity can be improved when reaching the theoretical material energy densities in the experiments. Therefore one can conclude, the expertise in a 3D technology should be enhanced to produce 3D-MBs for commercial use. One way of helping experimentalists to design 3D electrode geometries and study cell charge/discharge behavior is to use computer simulations of Li-ion batteries.

1.6 Computer simulations

As part of an effort to understand and investigate how physical or chemical processes evolve in the nature, scientists have developed a computational models that can result the analog dynamics of the behavior of the real system. A simulation uses a mathematical descriptions and functional relationships of the real model or problem and helps to describe ongoing processes which often are multiphysics problem solving. In general, simulations act as a bridge between experimental work and theory. The field of problems which can be modelled is very wide, starting from the atomistic scale of material modelling, human body movement simulations and up to weather forecasting. Most common simulation study includes the reference model with simulation results and modified model where one parameter is varied and impact tendency for the final results then can be identified. Furthermore, simulations allow us easily vary the geometrical parameters or make fundamental changes in the physical processes which experimentally can be time and resource consuming or even infeasible to carry out [48].

Theoretical study of the materials can be in different dimensionalities. Starting from material crystal structure modelling in the electronic level using Density Functional Theory (DFT) and going over to atomistic level, using Molecular Dynamics (MD), where optimal numbers of atoms 100 and 100000 can be simulated respectively [49]. DFT studies are used in practice to investigate the structural and electronic properties of molecules and defects. Since, the study accuracy is considerably high, the simulation timeframe is rather short, for example tens of femtoseconds [50] or picosecond. Somewhat larger system can be analyzed when using MD where simulation box is generally 1 to 100 nm and solver timestep is 1 fs which enables to visualize timeframes up to 1 ms. This method is mostly used for inspecting atomic changes and movements in the material structure and therefore helps to describe and explain material properties under various simulation conditions [49].

Differently from the previous studies, the Finite Element Method (FEM) is powerful tool to investigate larger systems in the macroscopic level [51]. Therefore, it allows to calculate and predict behavior of the entire system and moreover gives insights of the physical processes taking place in the material and thus makes most of the material properties observable. In the battery context, this method enables to describe ongoing electrochemical and thermal processes in the electrodes and thus estimates the battery performance and behavior under certain conditions. Here, FEM can be useful method for conducting theoretical studies of the Li-ion batteries and offer refinements for the experimental techniques of the cell preparation.

1.7 Scope of the thesis

The work presented in this thesis is focused on optimizing 3D-MB architectures via developing the simulation models and methodology. The aim of this research has involved the investigation of a fundamental understanding regarding several key aspects of different 3D battery architectures;

1. To gain deeper understanding of the ionic transport phenomena in these electrochemical cell components during charging and discharging, i.e. to conceive how the Lithium are detracted from the electrode material, ions transport occurs in the electrolyte and inserted into the opposite electrode.
2. To investigate how electrode geometry selection and electrodes dimensions variation influences the battery performance. In order to achieve maximum possible cell energy density together with uniform electrochemical activity of the electrodes and ionic transport in the electrolyte.
3. To understand the thermal behavior and temperature development in these 3D battery architectures and gaining insights how the temperature in turn influences the ionic transport in the cell and electrochemical processes in the active electrode material.

The goals of the research will be achieved by conducting computational simulations of the 3D-MBs using FEM. This approach allows to investigate full battery cells where all necessary material parameters for describing the physical conditions, thermal and electrochemical activity, is applied. Therefore, all ongoing processes in the battery cell during charging and discharging cycle should be taking into account to full fill all the criteria's for simulating working battery model. Such theoretical implementation of 3D microbattery allows to choose which cell architecture, electrode design and material is viable to achieve the best performance and highest cell capacity. Bellow follows a brief description of the studies conducted in this PhD project:

Paper I: FEM simulations of current distribution, material utilization in the electrodes and cell voltage development of a rechargeable Li-ion 3D MB, with concentric architecture. Time dependent simulations of a range of template pillar heights and interpillar distances have been performed and optimal electrode dimensions of the concentric architecture has been determined. The dynamics of the discharge curves, Li-ion concentration gradient for each cell design are compared between the different models during one full charge/discharge cycle. Shortest interpillar distance ($d = 10 \text{ mm}$) provides higher capacity per footprint area and an optimum pillar height is considered to be ca. 70 mm.

Paper II: Extensive simulations with a fully coupled 3D thermal-electrochemical model of 3D-MBs using FEM. 3D-MB architectures comprising pillar shaped, plate shaped and concentric electrode arrangements are simulated, using LiCoO_2 and graphite as a positive and negative electrode respectively and solid polymer electrolytes with LiTFSI salt. Complete 3D time-dependent description of the thermal behavior of the cells allows to investigate of thermal effects, thereby providing insights for optimization of the cell geometry in terms of both performance and safety.

Paper **III**: Experimentally-validated FEM has been used to simulate a 3D ordered macroporous carbon foam coated with LiFePO_4 for use as an electrode for 3D microbatteries. Geometrical factors affecting the electrode energy capacity are investigated. Modeling in this extent is expected to help in selecting the electrode material microstructural parameters required to optimize their electrochemical performance.

Present methodology provides insights into the various electrochemical aspects connected with these four proposed 3D-MB design ideas. Developed strategy allows to use parametric simulations of established electrochemical battery model, which helps to point out optimal electrode dimensions, geometrical designs and possible material selections. Thereafter experimental material preparation and techniques can be improved to increase the performance of the battery system.

2 METHODOLOGY

One way for solving problems of engineering and mathematical physics is to use numerical method called Finite Element Analysis (FEA) [51,52]. In this case laws of physics are expressed to describe the real-life phenomena, discretized equations are solved and results are analyzed, therefore the name FEA. One of the numerical method for solving formulas can be Finite Element Method (FEM). This method is typically used in structural analysis, heat transfer and also can be successfully used in the fluid flow and mass transport calculation. The dimensions of the research problem or investigated object may be in variety range, starting from 100 of nanometers up to tens of meters with time scales from microseconds up to hours and days. Therefore using nowadays computational power for FEM calculations, makes this technique to a perfect engineering tool for studying very complex problems as electrochemical processes and mass transport phenomena in the Li-ion microbatteries. This allows to benchmark performance of the battery with different electrode geometrical arranges and with different materials and properties and helps to design and optimize battery architectures.

2.1 Finite element method

Usually the laws of physics for describing the phenomena of interest are described by the partial differential equations (PDEs). These equations expresses a small change in a dependent variable due to the change in an independent variable (x,y,z,t) . Solving PDEs generally requires approximate numerical model equations and solutions using standard techniques (i.e. FEM) to calculate such approximations. Some of the problems for example which are described by the PDEs are conservation of thermal energy and conservation of mass. In this case heat transfer equation that expresses temperature changes in time and length is multiplied by the test function at both sides and obtained integration equation is called weak formulation. This systematic method converts the infinite dimensional function in to finite dimensional function and in turn to vectors which are numerically solvable. Since weak formula relaxes the PDE formula requirements the discretization has to apply for looking for approximated solution. Together with boundary conditions and discretization a matrix as a system of equations is obtained. The solution of the matrix with algebraic equations gives the approximation of the solution of the PDEs. Therefore higher discretization provides closer approximated solution to the real solution.

Typically accurate geometrical model is divided into a smaller and simpler subdomains called mesh elements. While solution is calculated in each position node of the mesh elements thus denser mesh provides also more accurate solution. Depending on the dimensionality of the computer model, different mesh elements can be used to discretize geometry. For example triangular and rectangular elements are used for 2D meshing and prismatic or tetrahedral elements

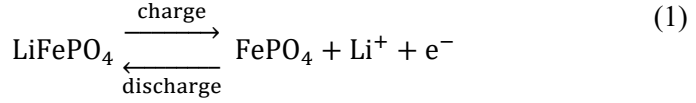
for 3D meshing. This approach allows to divide any geometry to a smaller domains where all the edges and boundaries can be perfectly defined. Most problematic shapes to mesh are the curved edges and thin regions since the element numbers are finite. Better conformity is achieved with smaller elements but higher mesh quality is usually related to the longer computation time. It is also important to choose mesh quality and thus elements size due to the engineering problem and used geometry thru mesh sensitivity study. Therefore, density of the computational points, solution quality and allowed error tolerance has to be estimated here considering general nature of the problem.

2.2 Electrochemical model of Li-ion batteries

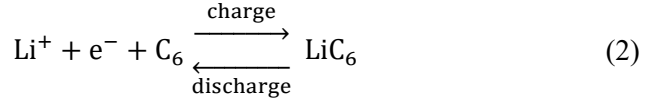
To model electrochemistry of the Li-ion batteries the current balance in the electrolyte, the current balance in both electrodes, the mass balance for the Li salt in the electrode and mass balance of Lithium in electrodes has to be described. General mass transfer from one location to other in solution phase is caused by the migration (gradient of electrical potential), diffusion (gradient of concentration) and convection (forced material flow) [53]. In most cases electrolyte can be modelled using two different approaches: dilute solution theory which accounts for electrochemical potentials and activity coefficients or concentrated solution theory where additionally concentration dependent diffusion has been taken into account. In this study concentrated solution theory is used and it is considered crucial in the Li-ion battery systems where single salt in the low resistivity homogeneous solvent is treated and thus exhibits concentrated behavior [5]. Concentrated solution theory is therefore the most common method for modelling mass transport in the liquid or polymer electrolyte of Li-ion batteries and bases on the Stefan–Maxwell diffusion equation, which has been reviewed by Newman and Tiedemann [5,54–57].

Usually electrodes in the Li-ion batteries have porous configuration, providing high surface area and thereby have increased electrolyte interface area for electrochemical reactions. This phenomena is described by the porous electrode theory where volume of the electrolyte in the porous electrode is defined as a fraction of the total electrode volume [58]. This theory also defines interactions of potential drop and concentration changes in both the solution and solid phase [5]. Additionally, Bruggeman's relations is used to describe effective ionic transport properties of the materials due to the porosity of the electrode for the Newman model [59].

In general at the interface between electrode and electrolyte the applied conventional electrical current as a flow of electrons in the electrode is converted into ionic current in the electrolyte and vice versa. During the charge process Li-ions are dissociated from the positive electrode and electrons are released. During discharge process Li-ions and electrons are deposited into the electrode, respectively:



The electrochemical reactions occurs opposite way at the interface between electrolyte and negative electrode:



The mathematical model of the Li-ion battery which describes all the natural electrochemistry occurring in the cell, can be very complex system. In that sense, catching all the processes and desired dependences of the battery chemistry in very detailed level can be sometimes over defining and unnecessary. Therefore, assumptions and simplifications are used in this study to keep model as simple as possible for modelling 3-dimensional Li-ion battery electrochemistry without reducing the value of the results thereat saving computational power. Model bases on the following general assumptions:

1. The porosity of the electrode is constant and material volume changes are neglected.
2. Electrode material particles are spherical with the certain mean diameter.
3. All pores of the electrode is filled with the liquid or polymer electrolyte.
4. System is free from convection.
5. Salt in the electrolyte is fully dissociated and all phases are electrically neutral.
6. Temperature effects are neglected in paper I and III.
7. Diffusion coefficients and ionic conductivities are constants in the electrodes and electrolyte with the exceptions in paper II and paper III where only electrical conductivity of the LiFePO_4 is concentration dependent function.
8. No electrochemical side reactions occur in the system.

While 3D-microbatteries are still under the development then only few studies present experimentally working full-cell prototypes. Moreover, 3D-MBs can have different architectures, geometrical configurations and material selection therefore, every system is unique and we have lack of experimental data to describe accurately all material parameters and full application behavior. However, appropriate model can be built and calibrated for detecting performance tendencies of the system when some geometrical or typical fundamental parameters are varied. Thus, established and reviewed models and well-studied materials should be used in the simulation system.

2.2.1 Li-ion transport in the electrolyte

Mass transport phenomena in the electrolyte is typically modelled with concentrated solution theory which bases on the Stefan-Maxwell multicomponent diffusion equation. The driving force for the Li-ion and anion transfer is the gradient of the electrochemical potential $\Delta\mu$ times concentration c_i of the specie i [57,60].

$$c_i \nabla \mu_i = RT \sum_j \frac{c_i c_j}{c_{tot} D_{ij}} (v_i - v_j) \quad (3)$$

Eq. 3 also formulates that driving force for specie i equals with the sum of friction forces acting on that specie which is expressed by the concentration times velocity difference of each pair of species ($v_j - v_i$). R is the universal gas constant, T is temperature (K), c_i and c_j are the concentration of the species i and j respectively, c_{tot} is the sum of the concentrations and D_{ij} is known as Stefan Maxwell diffusion coefficient for the interaction between the two species i and j .

By the electroneutrality condition, the mass balance for anions and Li-ions are identical i.e. ($c_+ = c_- = c$) and the molar flux N_+ (mol/m²s) of each Li-ion can be described as [5,61]:

$$N_+ = cv_+ = \varepsilon_l D \nabla c + \frac{i t_+^0}{z_+ F} + cv_0 \quad (4)$$

where D is the diffusion coefficient (m²/s) of the Li-ions in the electrolyte, i is the applied current density (A/m²) and t_+^0 is the electrolyte transference number of Li-ions, z_+ is the charge of the positive species, F is the Faraday's constant and v_0 describes the convection of the electrolyte.

According to the porous electrode theory, the porosity ε_l is the volume fraction of the electrolyte in the porous electrode. Porosity affects the interfacial area and concentration in the electrode volume and therefore change of the salt concentration in time can be expressed as [5,58]:

$$\varepsilon_l \frac{\partial c}{\partial t} = -\nabla N_s - R_i \quad (5)$$

where R_i is the reaction rate of the cation or anion per unit volume. When charge $z_+ = -z_- = 1$ and convection in the electrolyte is neglected, then the mass balance for Li-ions using effective diffusivity in both liquid and polymer electrolyte can be obtained by combining Eq. 4 and 5 [60,61]:

$$\frac{\partial c}{\partial t} = \nabla \cdot \left[(-D^{eff} \nabla c) + \frac{i t_+^0}{F} \right] - a_s j_{in} \quad (6)$$

where a_s is the area per unit volume (1/m) of the intercalation particles, j_{in} is the flux into the particles (mol/m²s) and the effective diffusion coefficient D^{eff} (m²/s) for the ions is formulated as [58,62]:

$$D^{eff} = D_e \varepsilon_l^\gamma \quad (7)$$

where ε_l is the electrolyte volume fraction of the porous electrode and $\gamma = 1.5$ is the Bruggeman's constant. Salt diffusion coefficient D_e of the electrolyte is related to the diffusion coefficients (m²/s) of the anion and cation respectively [5,60,61]:

$$D_e = \frac{2D_+D_-}{D_+ + D_-} \quad (8)$$

2.2.2 Electric potential in the electrolyte

The driving force for the species in Eq. 3 is the gradient of electrochemical potential μ_i which includes the potential gradient $\Delta\Phi$ and concentration gradient Δc_i . The electrochemical potential in the electrolyte for specie i can be determined by [61]:

$$\nabla\mu_i = RT\nabla\ln(c_i f_i) + z_i F \nabla\Phi \quad (9)$$

Where f_i is the activity factor and z_i is the charge of the specie. The potential Φ is the voltage of the electrode which is in contact with the electrolyte and is measured against the reference electrode. To express potential as a function of the Li-ions concentration c and current density i the Eq. 3 and 9 can be combined [5,61]:

$$\nabla\Phi = -\frac{i}{\kappa^{eff}} + \frac{2RT}{F} \nabla \left[(1 - t_+^0) + \left(1 + \frac{\partial \ln f_{\pm}}{\partial \ln c} \right) \ln c \right] \quad (10)$$

where κ^{eff} is the effective ionic conductivity (S/m) of the electrolyte, f_{\pm} is the average molar activity coefficient. Current density (A/m²) i in the electrolyte then can be expressed as [5,63,64]:

$$i = -\kappa^{eff} \nabla\Phi + \frac{2RT\kappa^{eff}}{F} \left(1 + \frac{\partial \ln f_{\pm}}{\partial \ln c} \right) (1 - t_+^0) \cdot \nabla \ln c \quad (11)$$

Bruggeman relation for the effective conductivity κ^{eff} is calculated as [62,65, 66]:

$$\kappa^{eff} = \kappa_e \varepsilon_l^\gamma \quad (12)$$

Ionic conductivity κ_e (S/m) can be defined as constant found from the literature or temperature and concentration dependent function for the liquid electrolyte modelled through the Nernst-Einstein equation (paper II) [60,61]:

$$\kappa_e = \frac{F^2 c}{RT} (D_+ + D_-) \quad (13)$$

The fundamental model for defining the transport kinetics in the electrolyte presented in the previous two subchapters can be therefore generally described by the three main physical properties: D_e diffusion coefficient (m^2/s), κ_e ionic conductivity (S/m), and transference number of the lithium ion t_{+}^0 .

2.2.3 Li-ion transport in the electrode

The electrochemical reaction Eq. 1 and 2 occur only on the surface of the spherical active material particle. Therewith, Li-ions as intercalant species diffuse towards the center of the particle and mass transport can be described by the Fick's second law [57]:

$$\frac{\partial c_s}{\partial t} = \nabla \cdot (-D_s \nabla c_s) \quad (14)$$

In this equation subscript s donates the electrode solid phase, c_s is the concentration (mol/m^3) of the intercalating species, t is time (s) and D_s represents the diffusion coefficient (m^2/s) of the Li-ion in the solid phase. This formula is solved as a 1D pseudo dimension equation where r represents the radial position within the particle and the governing equation can be written in spherical coordinates as [5,62,64,66]:

$$\frac{\partial c_s}{\partial t} = \frac{D_s}{r^2} \frac{\partial}{\partial r} \left(r^2 \frac{\partial c_s}{\partial r} \right) \quad (15)$$

With boundary conditions [5,62,66]:

$$\left. \frac{\partial c_s}{\partial r} \right|_{r=0} = 0 \quad (16)$$

$$D_s \left. \frac{\partial c_s}{\partial r} \right|_{r=r_p} = \frac{-j^{Li}}{a_s F} \quad (17)$$

where j^{Li} is the volumetric rate of reaction at the particle surface, a_s the interfacial surface area ($1/\text{m}$) is calculated as:

$$a_s = \frac{3\varepsilon_s}{r_s} \quad (18)$$

Where $\varepsilon_s = 1 - \varepsilon_l$ is the solid phase volume fraction of the porous electrode and r_s is the radius of the spherical active material particle. In this context, only diffusion within the active material particle is assumed. The Li-ion diffusion between particles is neglected since the distance between particles are considered much larger than length scale of the particle. In addition, constant diffusion coefficient D_s of each electrode material respectively was used in these simulations where values was found in the literature and are presented in the papers.

2.2.4 Potential in the electrode

Electrons are transferred from external circuit in to the current collector of the electrode. The electrons transport in the porous electrode solid phase is driven by the electrical potential gradient $\Delta\Phi$ of the electrode and is determined from Ohm's law [5,64]:

$$i_s = -\sigma_s^{eff} \nabla\Phi_s \quad (19)$$

where i_s is the current density (A/m²) in the electrode and σ_s^{eff} refers to the effective electronic conductivity (S/m) in the solid which is corrected for the volume fraction of the electrode by the Bruggeman's relation [62]:

$$\sigma_s^{eff} = \sigma_s \varepsilon_s^\gamma \quad (20)$$

Where σ_s is the electronic conductivity (S/m) of the electrode.

2.2.5 Electrochemical kinetics

At the interface between electrolyte and electrode, the ionic concentrations Eq. 6, Eq. 14 and potentials Eq. 10, Eq. 19 in the solution and solid phase respectively are coupled together by the Butler-Volmer electrochemical kinetic expression. Therefore, the intercalation current density J which relates the rate of reaction, overpotential and concentration on both electrodes can be modelled as [65,66]:

$$J = i_0 \left[\exp\left(\frac{\alpha_a F \eta}{RT}\right) - \exp\left(-\frac{\alpha_c F \eta}{RT}\right) \right] \quad (21)$$

where α_a and α_c are the anodic and cathodic transfer coefficients. η is activation overpotential (V) for electrode reaction and is formulated as a potential difference between solid φ_s and electrolyte φ_l phase minus the thermodynamic equilibrium potential U_{eq} of the solid electrode phase [66,67]:

$$\eta = \varphi_s - \varphi_l - U_{eq} \quad (22)$$

Exchange current density i_0 in Eq. 21 is expressed as [5,64,66]:

$$i_0 = F(k_a)^{\alpha_c}(k_c)^{\alpha_a}(c)^{\alpha_a}(c_{s,max} - c_s)^{\alpha_a}(c_s)^{\alpha_c} \quad (23)$$

where k_a and k_c are the anodic and cathodic kinetic rate constants (m/s), $(c_{s,max} - c_s)$ is the concentration (mol/m³) of unoccupied sites in the particle and c is Li-ions concentration in the electrolyte.

2.3 Thermal model of Li-ion batteries

Heat generation in the electrochemical cell is the summation of heat sources and sinks in the two electrodes, electrolyte and at the current collector interfaces. Heat is generated by reversible or irreversible heating. Reversible heat is related to the entropy change of the electrochemical reaction in the electrodes which can be endothermic and exothermic processes. Irreversible heating on the other hand is connected to the charge transfer as Ohmic losses and mass transfer limitations in the solid and liquid phase.

The energy balance has to be considered in the system, therefore heat generation Q and temperature T changes are related and heat transfer can be determined as follows [14,68]:

$$\rho C_p \frac{\partial T}{\partial t} = \nabla \cdot (k \nabla T) + Q \quad (24)$$

where ρ is density (kg/m³), C_p is heat capacity (J/(kg·K)) at constant pressure, t is time (s) and k is thermal conductivity (W/(m·K)). The heat sources and sinks Q , (W/m³) in the electrochemical cell can be define by the three main phenomena.

$$Q = Q_{rev} + Q_{JH} + Q_{cc} \quad (25)$$

Reversible heating Q_{rev} (W/m³) due to the electrochemical reactions because of the entropy change ΔS can be expressed as [5,64,68]:

$$Q_{rev} = -IT \frac{\partial U_{eq}}{\partial T} = -T \Delta S \frac{I}{nF} \quad (26)$$

where current (A) is defined as I and $\partial U_{eq}/\partial T$ is the function that describes the temperature derivative of open circuit potential which in turn is state of charge (SOC) dependent.

Joule heating Q_{JH} (W/m³) describes the heat generated by the ohmic losses in the solid phase and by charge transport in the liquid phase [64,69]:

$$Q_{JH} = I(U_{eq} - U) = -i_s \cdot \nabla \varphi_s - i_l \cdot \nabla \varphi_l \quad (27)$$

where i_s and i_l are the current densities, φ_s and φ_l are potential (V) in the solid and liquid phase respectively.

The heat generation due to the current collector contact resistance is calculated by [70]:

$$Q_{cc} = I^2 \frac{R_{cc}}{a} \quad (28)$$

where current collector resistance $R_{cc} = 20 \Omega$, and a is the current collector contact surface area (m^2).

Temperature (K) and concentration (mol/m^3) dependence for the diffusion coefficient in the liquid electrolyte (Paper II) from the references is defined with the estimated polynomial function [14,64,71]:

$$D_e(c, T) = 10^{(-7.43 - (\frac{54}{T - 229 - 5 \times 0.001c}) - 0.22 \cdot 0.001c)} \quad (29)$$

Temperature dependent ionic diffusion coefficient for the polymer electrolyte (paper II) is described through the Vogel-Tamman-Fulcher (VTF) expression [5,72]:

$$D_e = \frac{A}{T^{1/2}} \exp \left[\frac{-E_a}{k_B(T - T_0)} \right] \quad (30)$$

where A is concentration dependent pre-exponential factor, T is temperature (K), E_a electrolyte pseudo-activation energy (eV), k_B is the Boltzmann constant and T_0 is the “ideal” glass transition temperature with the typical value of ($T_g - 50$) [73,74].

Temperature dependent ionic diffusivity and electrochemical reaction rate for the both LiCoO_2 (LCO) positive electrode and graphite negative electrode (paper II) is described using the Arrhenius type relation:

$$\Psi = \Psi_0 \exp \left[\frac{E_a(T - 293)}{293 \cdot RT} \right] \quad (31)$$

where Ψ is either initial value of the diffusivity (m^2/s) or reaction rate (m/s) at 293 K, E_a is the activation energy (J/mol) and R is the universal gas constant. All specific parameters are defined in the table 2 (appendix section).

2.4 Simulated 3D-MB architectures and materials

All investigated micro battery geometries in this thesis have simulated as 3-dimensional models. This 3D approach need more computational power but in turn takes account more precise ionic movements and geometrical aspects and thus can provide more detailed information and realistic cell performance. Here four different MB cell architectures are studied: 3D-interdigitated, 3D-trench, 3D-concentric and aperiodic foam respectively as described previously in the Figure 3. Interdigitated and concentric designing ideas bases on the pillars that are placed periodically on the planar electrode to increase electrode electrolyte surface area. The difference between interdigitated and concentric architecture is that one have both negative and positive pillared electrodes and another have only one electrode pillared and opposite electrode is defined as the rest of the volume respectively besides the thin layer of electrolyte between the electrodes as shown in the Figure 4. The performance of the 3D-concentric architecture with various geometrical dimensions is studied in the paper I. Trench architecture is one of the electrode design that uses plates instead of pillars on the both planar electrodes to increase surface area. Performance and thermal effects of all three architectures are simulated and compared in the paper II. Aperiodic structure on the other hand uses 3D-foam type electrode and this half-cell with liquid electrolyte is simulated and insights of the electrochemical behavior of that type novel electrode are described in the paper III.

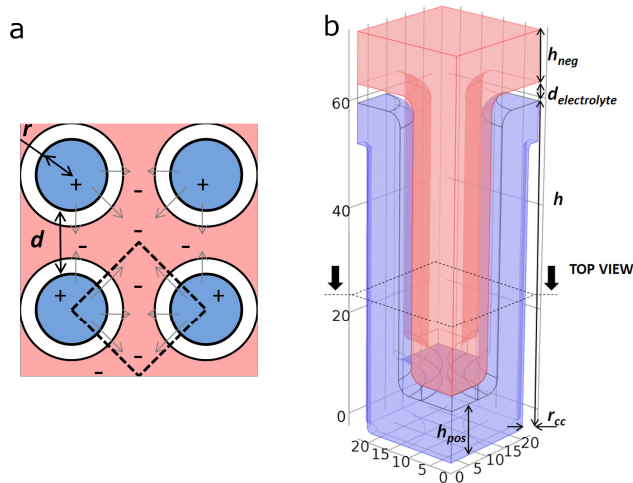


Figure 4. Representation of the Li-ion cell with the concentric architecture where blue presents the positive electrode LCO and red is negative electrode (graphite). (a) Schematic top view of the architecture with gray arrows highlighting the electrical field and totted box shows the actual simulated section. $r = 10 \mu\text{m}$ is radius of the pillar and d is varied interpillar distance. (b) Simulated cell (reference system) with interpillar distance of $12 \mu\text{m}$, pillar height $60 \mu\text{m}$, thickness of the electrolyte $d_{\text{electrolyte}} = 3 \mu\text{m}$ and thickness of the electrodes base layer (h_{neg} and h_{pos}) is $10 \mu\text{m}$.

Materials used in these studies are well known and previously widely studied electrode materials which are still used in the commercial batteries. Lithiated graphite (LiC_6) is modelled as a negative electrode and LiCoO_2 as positive electrode in the both paper I and II. Carbon allotrope graphite is mostly utilized as a negative electrode due to the high electronic conductivity and high practical capacity of approximately 350 mAh/g [6,75]. Additionally, cyclic curve of the graphite in Li-ion batteries have much flatter profile with the low operating potential of 0.125V providing wide and stable electrochemical window. LiCoO_2 is broadly used as a positive electrode material due to the high enough theoretical capacity (270 mAh/g) for portable devices. However, for reversible usage only half of the Li-ions ($0.5 < x < 1$ in Li_xCoO_2) can be electrochemically extracted from the lithiated cobalt oxide because of the irreversible morphological changes in the structure, which brings the practical gravimetric capacity down to ~140 mAh/g [16,76]. The Lithium intercalation/extraction occurs typically at high plateau, around 3.9 V against Li/Li^+ reference electrode. Working voltage window for such LiCoO_2 and graphite, C, cell is usually from discharge state 3.5 V up to 4.1 V at the charged state. Electrolyte in these studies are considered to be solid polymer type (poly(ethylene oxide); PEO) with the 1M LiPF_6 salt and 1.5 M LiTFSI salt in the paper I and paper II respectively.

In paper III Li-ion half-cell consisting LiFePO_4 (LFP) positive electrode is studied. LFP nanoparticles are coated conformally on the porous carbon electrode acting as a thin layer of positive electrode as shown in Figure 5a, 5b and 5d. In this case similar geometrical model of the electrode structure is created (Figure 5c). For simulations small fraction of this foam type lithiated electrode is soaked into the liquid electrolyte (1 M LiPF_6 in 1:1 ethylene carbonate : dimethyl carbonate (1:1 EC:DEC)) and is discharged against the Li-metal electrode as shown in the Figure 6. Li_xFePO_4 is usually cycled in the range ($0.1 < x < 1$) which makes this electrode material rather stable with the (dis)charge voltage at 3.4 V [16]. The gravimetric capacity of the LFP is up to 153 mAh/g which is somewhat higher than the practical capacity of the LiCoO_2 .

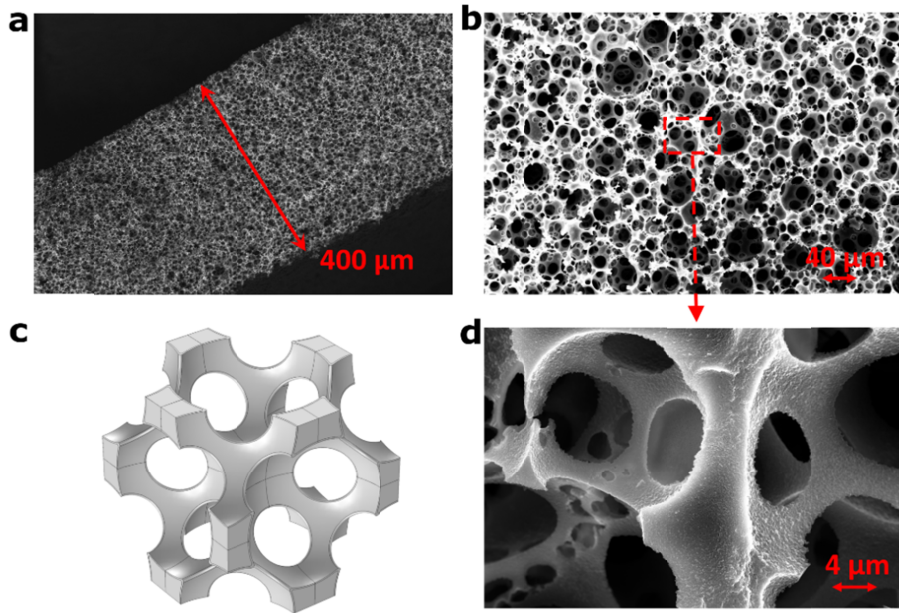


Figure 5. (a) Section of the foam type electrode with the thickness of 400 μm . Micrographs (b) and (d) corresponds to the electrode structure morphologies in a higher magnification. (c) Represents the computer model of that electrode structure with the 200 nm thick LiFePO_4 coating.

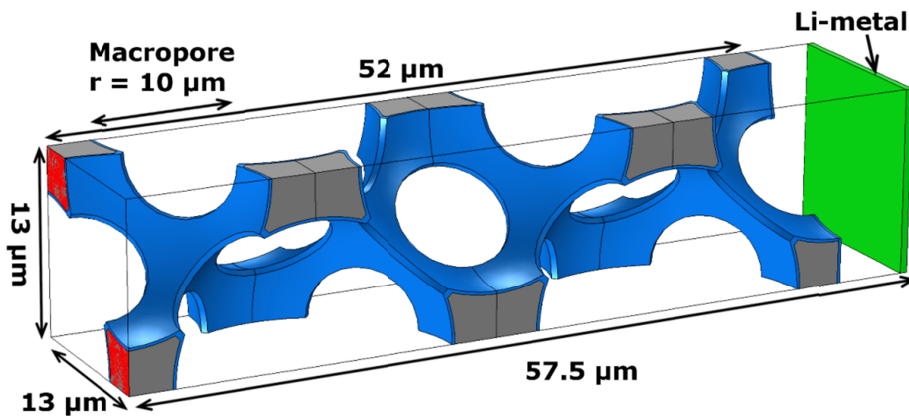


Figure 6. Simulated half-cell of the carbon structure (gray) coated with 200 nm thick LiFePO_4 layer (blue). Current is applied on the red area and Li-metal sheet (green) is grounded. The rest of the volume is filled with the liquid electrolyte.

3 RESULTS AND DISCUSSION

3.1 General charge-discharge characteristics of the 3D-MB

Voltage development, also named as charge/discharge curves or profiles of the conventional 2D Li-ion batteries and 3D microbatteries during the cycling are usually similar and have typical characteristics because of the electrochemical reactions occurring in the cell. In example potential development during charging and discharging cycle of the 3D microbattery with concentric architecture is shown in the Figure 7. Current density of 4 A/m^2 was used to charge this microbattery consisting of pillars with the interpillar distance $d = 12 \text{ }\mu\text{m}$ and pillar height $h = 60 \text{ }\mu\text{m}$ from 3.5 V up to 4.1V and thereafter the cell was discharged from 4.1 V down to 3.5 V. The characteristic difference of the charge and discharge profile is mainly due to the IR drop and activation polarisation loss at the beginning of the discharge cycle. During charging and discharging smoothly rising and lowering cell potential is sum of the potentials on both electrodes which in turn is a function of state of charge respectively in both electrodes and is caused by the Ohmic losses in the electrodes and due to the concentration polarization in the electrolyte [8,75]. Additionally, sudden potential drop of the cell at the end of the discharge corresponds to depletion of the electrode materials [5,77]. The shape of the potential curve is similar to those found in the literature where also 3D electrodes were studied [77–79] and correspond to the estimated behavior for the graphite/LiCoO₂ cell chemistry [62,80]. This similarity therefore indicates that the simulated model accurately captures the electrochemical activity in the cell and can be therefore used to describe the mass and charge transport phenomena and benchmark different MB architectures.

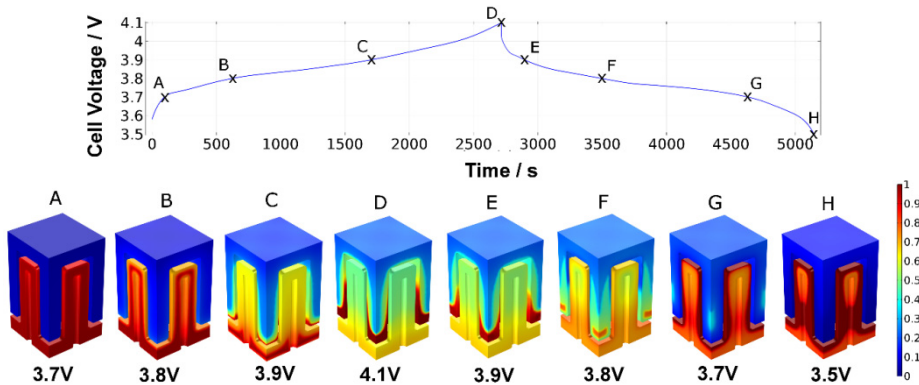


Figure 7. Charge/discharge potential profile of the concentric 3D-MB and state of charge (x in Li_xCoO_2 and Li_xC_6) in the positive and negative electrode respectively at different cell voltage stage during the one full cycle.

Snapshots of the state of charge as a degree of lithiation in the electrodes taken at certain cell voltage values during the one simulated full cycle is presented in Figure 7. This provides direct insights into the Lithium distribution in both electrodes and describes the electrode material utilization in the certain 3D-MB architecture. Initially positive pillared electrode (LiCoO_2) is fully ($\sim 98\%$) lithiated and opposing electrode graphite has fully delithiated. During charging Li-ions are detracted from the positive electrode and are inserted into the electrolyte. Hereby the concentration start to increase in the electrolyte near the positive electrode and ions start to diffuse towards the negative electrode and are inserted in the negative electrode as seen in snapshot C. It has to be noticed that LCO delithiation is rather uniform compare to the lithiation of the negative electrode that preferably occurs in the tips of the electrode which are near to the base layer of the positive electrode. Such non-uniform lithiation in the graphite can possibly occur due to the differences between electrodes surface areas and volumes (graphite tips against LCO pillars near the base layer) in these regions and that graphite electrical conductivity is 10^3 times higher than LCO in this simulation. It can be seen that local current density distribution in positive electrode is rather homogeneous and therefore the electrochemical activity at the beginning of the charging cycle in turn provides homogeneous ionic flux over the surface of the LCO electrode. However, at later charge phases i.e. C and D the more non-uniform delithiation and lithiation develops in the positive and negative electrode, respectively. LCO pillar tips becomes more electrochemically active possibly due to the graphite tips depletion and significantly smaller volume of the positive electrode in the tips of pillar than volume of the graphite in this region. Also base layer of the positive electrode appears to be less active and leads to inhomogeneous current density distribution throughout the electrode in this architecture.

During discharge (from D to H) positive pillared electrode is lithiated and it can be seen that distribution of the lithiation is rather uniform with the exception in the pillars near the base layer that are lithiated somewhat faster (G and H). Same time delithiation in the tips of the graphite electrode is more intense than it is in the base layer. It is interesting to note that at the end of the cycle top part of the LCO pillar near the pillar current collector surface has somewhat lower lithiation stage that it was at the beginning of the charge cycle (evenly $\sim 98\%$). LCO electrode is first fully lithiated near the surface and then Lithium diffuses inside the bulk. It can be considered that more uniform lithiation can be achieved when electrolyte has higher ionic conductivity or lower current density is used.

3.2 Benchmarking different architectures for 3D-MBs

For characterizing 3D microbattery performance and capacity of the cell with different electrode configuration, three models of previously proposed 3D architectures (interdigitated, concentric and trench) using graphite and LCO electrodes was built and full cycles was simulated. In Figure 8 discharge voltage

profiles of each system for current densities (1 and 10 A/m²) and gravimetric capacity (mAh/g) per gram of positive electrode material (LCO) is presented.

It can be seen that potential development is similar in all the systems where potential decreases smoothly during discharging with the sudden potential drop around cell voltage of (3.6 V) that is realistic and common behaviour as discussed in previous section. Higher current density (10 A/m²) evoke deeper voltage drop at the beginning of the discharge in all the systems because of the Ohmic losses and polarization effect and is deepest in the trench architecture (Figure 8c). Furthermore, it can be noticed that trench architecture exhibit somewhat lower potential values compared to the other systems and also lowest cell capacity in all current density values. This can be due to the electrode/electrolyte surface area differences in these systems. Since cells with pillars (interdigitated and concentric) have higher electrode surface area per electrode footprint area than in system with trench electrode configuration. Higher electrode/electrolyte surface area in principle should provide lower local current densities, deeper lithiation/delithiation and smaller polarisation. This lower performance is studied in more detailed in the section 3.5 where thermal effects and temperature dependences are included in the battery simulations.

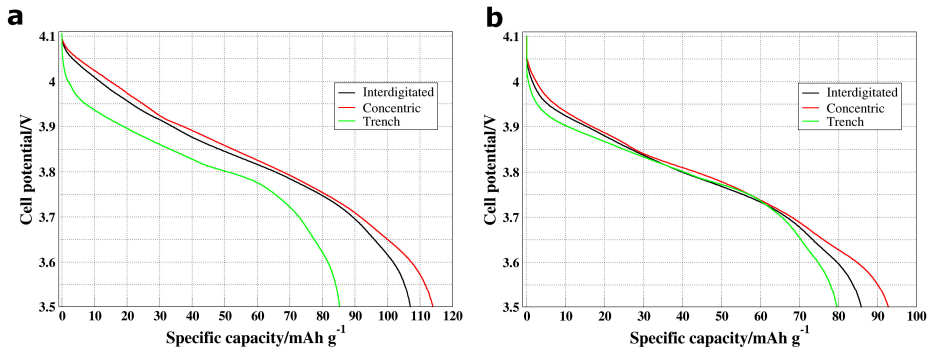


Figure 8. Cell voltage profiles of different 3D-MB architectures during discharge at various current densities: a) 1 A/m² b) 10 A/m².

When comparing gravimetric capacities in these cells at different current densities then interdigitated and concentric architectures delivers similar results. Still somewhat lower capacity value 107 mAh/g was achieved when interdigitated electrode configuration is used under 1 A/m² discharge current density. Highest performance with capacity of 114 mAh/g at 1 A/m² was found in the concentric type cell. However, one magnitude higher current density reduces the cell capacity by 18% in this architecture. Since the highest cell capacity was achieved in the concentric cell then parametric simulations with varying electrode geometrical dimensions will be studied which can provide significant insights about mass transport in the cell and suggest optimal electrode dimensions for the best battery performance.

3.3 Optimization of the electrode dimensions in concentric architecture

3.3.1 Variation of pillar heights

To find out viable electrode pillar height for concentric architecture to achieve optimal performance, four different configuration (pillars heights: 40, 60, 80 and 100 μm) was built and full cycle was simulated. Time dependent discharge profiles for the first discharge cycle (from 4.1 V down to 3.5 V) of these geometries are shown in the Figure 9. It is visible that sharpest potential drop is in the system with the shortest pillars (40 μm) while constant current density 4 A/m^2 per cell footprint area was used. This can be due to the higher local current densities arising in the short pillared system (40 μm) because of 2.7 times smaller positive electrode surface area compare to the positive electrode surface area of the 100 μm pillars system. Higher pillars should therefore provide a lower current densities and more distributed current over the larger electrode surface and thus more homogeneous electrochemical activity. Furthermore, higher imbalance between the lithiation levels in the positive and negative electrode in the system with smaller pillars can cause a large flux of Li-ions due to the high current rates at the beginning of the discharge. This polarization effect was also mentioned in the section 3.2 when different current densities was applied in these systems.

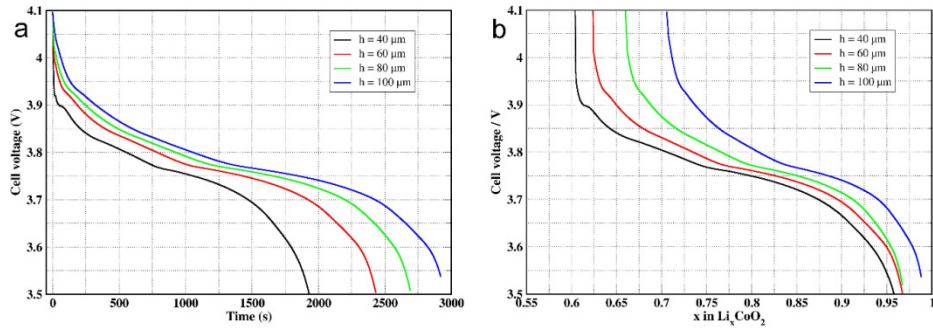


Figure 9. Discharge cycles after charging of the concentric architecture with the 12 μm interpillar distance and different pillar heights (h) using constant current density of 4 A/m^2 : (a) Discharge curves of the cells. (b) Degree of lithiation in the Li_xCoO_2 electrode.

It can be seen (Figure 9) that discharging duration in these systems varies between 1900 and 2900 seconds and apparently higher pillars with larger amount of electrode material increases the discharge time and thus cell capacity per footprint area escalates. On the other hand system with shorter pillars (40 μm) have half (53 %) the LCO electrode mass loading compare to positive electrode in the

100 μm system but the discharge time is only 35 % reduced. This states that deeper LCO delithiation (previous cell charging) occurs in the system with shortest pillars where LCO lithiation starts at the level of around $\text{Li}_{0.60}\text{CoO}_2$ (delithiation state when the cell is fully charged). High pillar system on contrary provide only approximately $\text{Li}_{0.71}\text{CoO}_2$ depth of delithiation in the LCO electrode. Deeper LCO delithiation and enhanced material utilization in 40 m pillar system can be caused by the shorter transport pathways for ions. While the shortest ionic transport pathway is approximately the thickness of the electrolyte then longest pathway however in extreme cases can be the distance between base layers of both electrodes. Therefore, shorter charge transport pathways leads to the lower cell resistivity and vice versa. When high pillars are used, internal resistance of the cell increases and more energy is lost for ionic transport, which in turn causes potential drop on the wired cell and therefore lower local currents occur and part of the active material remains underutilized. Again, shorter pillars provide deeper LCO delithiation and higher active material utilization while higher pillars with somewhat improved overall capacity is reached at the cost of underutilized regions in the cell.

To illustrate the depth of delithiation and mass distribution in the LCO electrode the delithiation states for different pillar heights at the beginning of the cell discharge (therefore at the end of the charging) process are plotted in the Figure 10. As mentioned previously, shorter pillars with less amount of material provide overall deeper LCO delithiation and better material utilization. However, it has to be point out that deepest delithiation $\text{Li}_{0.49}\text{CoO}_2$ in the tips of the pillar and minimum level of $\text{Li}_{0.70}\text{CoO}_2$ in the base layer makes the delithiation distribution most inhomogeneous in the 40 μm pillar system. This combination can be caused by the smaller amount of active material that is relatively closer to the opposing electrode and thus smaller surface area with shorter pathways (also in negative electrode) thereby decreases electronic resistance and ionic diffusion time and delivers higher current density and deeper degree of delithiation can be achieved.

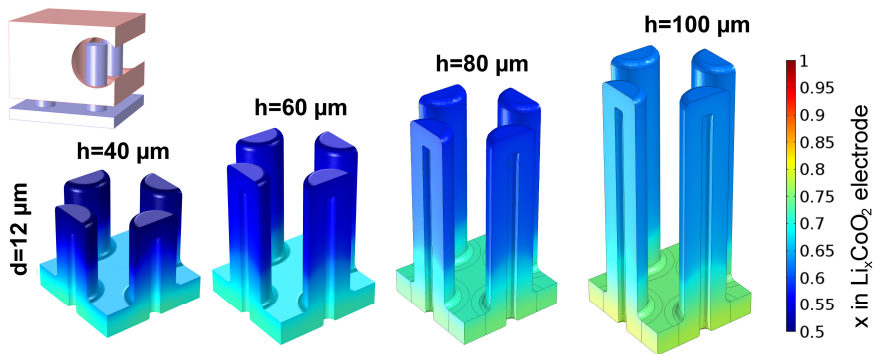


Figure 10. Depth of delithiation (x in Li_xCoO_2) in the positive electrode at the beginning of the discharge (after charging of the cell) with different pillar heights.

In contrast, 100 μm pillar system with larger electrode surface area and lower local current densities provides a more homogeneous current flow and therefore leads to the most homogeneous delithiation with maximum depth of delithiation of $\text{Li}_{0.67}\text{CoO}_2$ and minimum value of $\text{Li}_{0.77}\text{CoO}_2$ which is smallest difference among these systems. Nevertheless, the delithiation in the pillars is uniform, the base layer on positive electrode is not so electrochemically active since the tips of the negative counter electrode has much smaller volume in this part of the cell. To reach complete material utilization, sufficient electronic and ionic conductivities has to support mass transportation thru the ionic pathways that have same distance length between electrodes and also active material distribution in the electrodes has to provide viable volumetric capacity for Li-ions.

Li-ion concentration gradient in the electrolyte for 100 and 60 μm pillar height systems at certain cell voltage stages (4.1, 3.9, 3.8, 3.7, 3.5 V) during discharging are presented in Figure 11. The concentration gradient highlights the regions where intense increase or decrease of the Li-ion concentration is taking place. Therefore, ionic movement due to the combined effect of diffusion and migration highly characterizes the current density and electrochemical activity in nearby regions. It is visible that concentration gradient is much higher at the bottom of the positive electrode pillar near the base layer where is also tip of the graphite electrode located. This effect is strongest at the beginning of the discharging and stays in both systems during around half of the discharging time and afterwards the concentration gradient homogenizes gradually in the electrolyte. It can be assumed that this behavior is caused by the differences between the lithiation level in the fully lithiated tips of the graphite electrode (Figure 7d) and LCO electrode and furthermore by the SOC differences between LCO base layer and pillars. As delithiation proceeds, the delithiation process in the graphite tips becomes slower and more uniform ionic flux develops in the electrolyte between the electrodes.

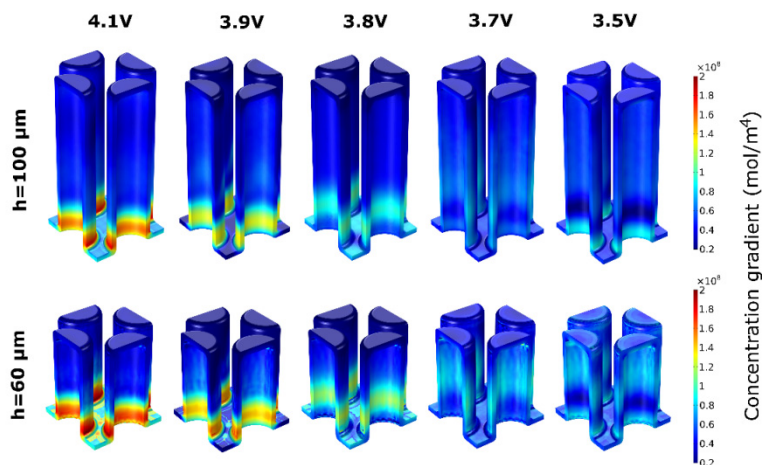


Figure 11. Concentration gradient in the electrolyte of the system with pillar height 100 μm (top row) and reference system with pillar height 60 μm at different cell voltage stages during discharge.

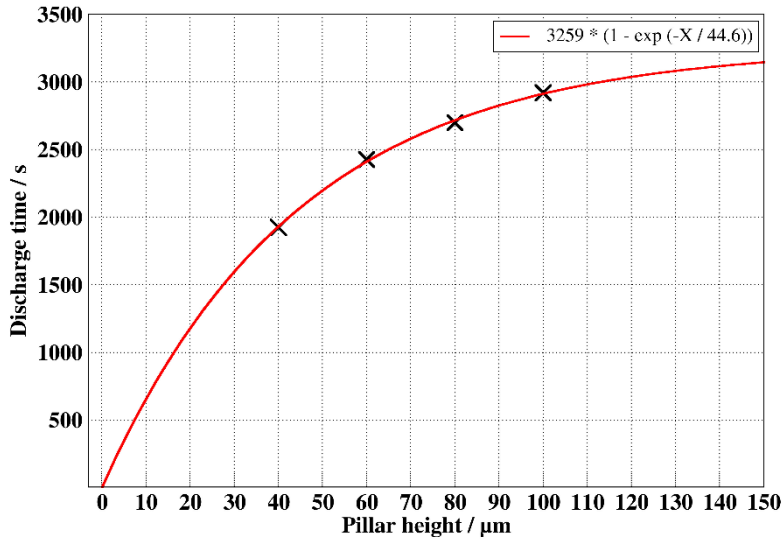


Figure 12. Discharge time for different concentric architecture with different pillar heights (crosses) and fitted exponential function.

When comparing concentric architecture performances as discharge duration in these simulated cells with different pillar heights (Figure 12) at constant current density of $4 \text{ (A/m}^2\text{)}$ then the results can be described by the exponential dependence. As the pillar height increases the discharge time enhances and therefore exists the trade-off between cell capacity gain per footprint area and convenient electrode material usage. In addition, higher pillars provide more homogeneous delithiation/lithiation of the positive electrode and thus should have better rate capabilities. Smaller pillars on the other hand, deliver deeper possible delithiation in LCO electrode which improves material utilization. Still it is challenging to estimate which system possess better effective capacity from the fitted exponential curve. Still it should be mentioned that considerable capacity gain is in the system using up to $70 \mu\text{m}$ height pillars, which might be the optimum value for the concentric cell design.

3.3.2 Variation of interpillar distance

Another set of simulations describes the effects of varying the interpillar distances of ($10, 12, 16, 20 \mu\text{m}$) in the concentric MB architecture while the pillar height was kept constant $60 \mu\text{m}$. It is somewhat surprising that discharge profiles in Figure 13a show almost identical results where discharge time varies merely between 2375 and 2450 seconds. In these studied geometries, only area of the base layer changes and thus volume of the positive electrode changes (1.28 times larger material loading for the $d = 20 \mu\text{m}$ than in the $d = 10 \mu\text{m}$ system) while

difference between both electrode surface areas stays same in these systems. Key effect between these geometries is the average state of charge in the positive pillared electrode at the beginning of the discharge cycle (at the end of the LCO delithiation) that can be seen in the Figure 13b. System with longer interpillar distances ($d = 20 \mu\text{m}$) have average delithiation level $\text{Li}_{0.67}\text{CoO}_2$ throughout the electrode while the shortest interpillar distances provide $\text{Li}_{0.60}\text{CoO}_2$ and therefore are capable for sustaining better material utilization.

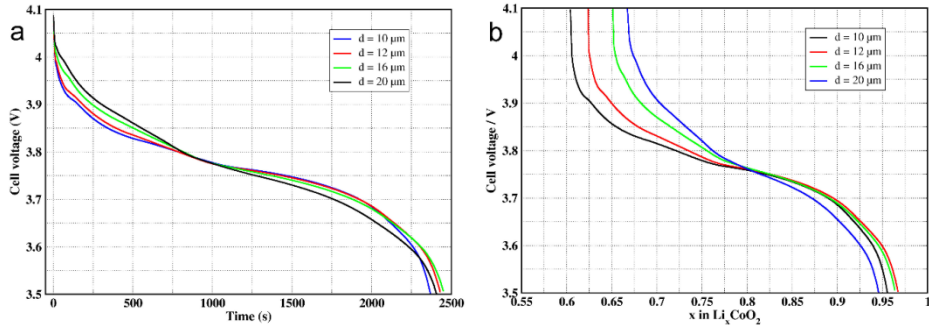


Figure 13. Discharge cycles after charging of the concentric architecture with the $60 \mu\text{m}$ high pillars and different interpillar distances (d) using constant current density of 4 A/m^2 : (a) Discharge curves of the cells. (b) Degree of lithiation in the Li_xCoO_2 electrode.

For deeper understanding, graphical illustration of more detailed delithiation distribution in the LCO electrode has presented in Figure 14. In $d = 10 \mu\text{m}$ system the deepest delithiation of $\text{Li}_{0.48}\text{CoO}_2$ presents in the tip of the pillar and lowest delithiation state $\text{Li}_{0.73}\text{CoO}_2$ in the base layer near the current collector. Geometry with longest interpillar distance $d = 20 \mu\text{m}$ on the other hand shows smallest difference between maximum $\text{Li}_{0.70}\text{CoO}_2$ and minimum $\text{Li}_{0.61}\text{CoO}_2$ level of delithiation in the LCO electrode at the beginning of the discharge cycle and is therefore indicating more uniform delithiation. Such nonhomogeneous delithiation in the system with more tightly packed pillars can be caused by the higher non-uniformities in the cell due to the closer pillars and narrow negative electrode regions between. This setup causes more non-uniform local current densities appearing in the active material and thereby referring to the higher concentration gradients in the electrolyte. Since electrochemical reaction in the graphite occurs preferably on the particles near the electrode surface, Lithium diffuses into the particles and towards the deeper particles rendering growing depletion layer. Therefore, thinner regions of the negative electrode are depleted in forehand compare to the thicker negative electrode regions. Thus, closer pillars with shorter ionic pathways and higher local current densities have likely lower cell resistance and deeper delithiation can be obtained. However, it should be noted that system with closest pillars provide sufficient negative

electrode material between the pillars for deep LCO delithiation which can be possible due to the high enough electrical conductivity of the graphite.

When comparing these geometries, then electrode volume per cell footprint area should be taken into account. When these studied geometries provide similar capacities then per footprint area (i.e. 1 mm^2), the $d = 10 \text{ m}$ system provides higher pillar density and this translates into increased active material usage. In conclusion, although longer interpillar distance shows more homogeneous delithiation, the system with closer pillar clearly offer deeper LCO delithiation with better material utilization and increased capacity due to the higher material loading per cell footprint area.

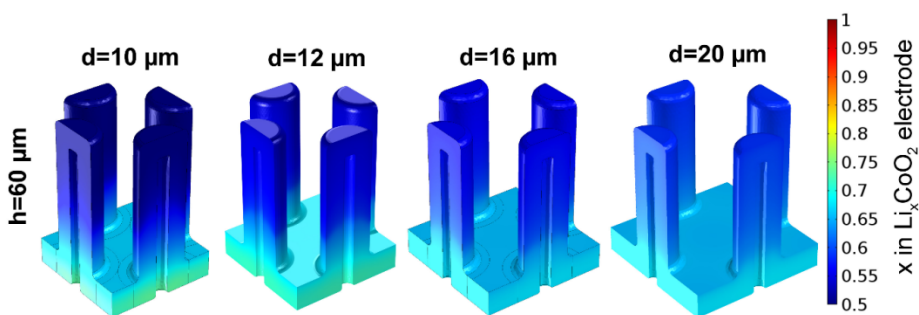


Figure 14. Depth of delithiation (x in Li_xCoO_2) in the positive electrode at the beginning of the discharge (after charging of the cell) with different interpillar distance.

3.4 Parametric studies of the aperiodic MB architecture

3.4.1 Charge characteristics

One of the novel electrode material is a high surface area carbon foam which can be used in 3D structured batteries (Figure 5) [47]. Here, 3D composite positive electrode fabricated from LiFePO_4 nanoparticles deposited conformally on carbon foam is simulated and characterized. 3 different current densities (0.1 , 1 and 3 mA/cm^2) was applied to the cell which roughly corresponds to the 0.06 , 0.69 and 2.44 C-rates . The simulated cell voltage curves are presented and compared respectively with the experimental data in Figure 15. Close agreement between simulated and experimental results indicates that developed model can accurately capture the mass and charge transport phenomena in this system. Therefore such validated model can be used to obtain reliable insights into the electrochemical behavior of the microbatteries with 3D foam type electrode.

These cell voltage profiles (Figure 15) with the flat potential plateau are typical for the cells using LiFePO_4 electrode. The horizontal potential plateau level depends strongly on the applied current density where lower charge rates induces lower local currents and therefore smoother and deeper delithiation. In this half-cell with LiFePO_4 coated carbon foam, the level of delithiation $\text{Li}_{0.04}\text{FePO}_4$ and capacity of 160 mAh/g was reached which is 94% of the

LiFePO₄ theoretical capacity (170 mAh/g) using current density of 0.1 mA/cm² [81]. Higher current density (3 mA/cm²) on the other hand shows 26 % lower cell capacity (118 mAh/g) and depth of delithiation was Li_{0.3}FePO₄. Also similar potential curves and depth of delithiation Li_{0.2}FePO₄ has been reported previously [82,83]. It can be that under high charging rates, electrolyte due to the long distances may become polarized and some portion of the LiFePO₄ particles are not participating fully in the delithiation process and thus charging is impeded. Low charging rates on the other hand provides sufficient diffusion in the electrolyte to maintain homogeneous delithiation and uniform charging at all depths in the porous electrode. Therefore, using LiFePO₄ in this foam type electrode design is a good achievement and gives promising results under low charging/discharging rates.

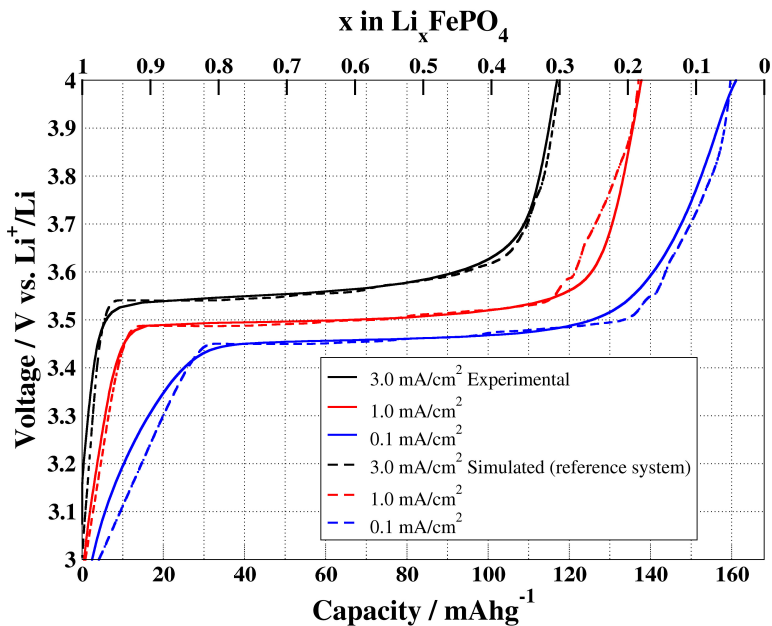


Figure 15. The cell charge voltage-capacity profiles of LiFePO₄ coated carbon foam at different current densities (solid and dotted lines indicates experimental and simulated results, respectively). Upper horizontal axes presents degree of delithiation (x in Li _{x} FePO₄), lower horizontal axes shows cell gravimetric capacity.

3.4.2 Current density in the carbon and concentration gradient in the electrolyte

Current density (A/m²) distribution in the carbon foam structure at the end of the charging cycle is shown in Figure 16a. It should be mentioned that current density distribution in the carbon foam remains same during the cycle due to the constant charging 2.44 C-rates applied. When LiFePO₄ delithiation (Equation 1)

occurs then all detached electrons from electrochemical reaction are inserted into the carbon structure from LiFePO_4 contact interface area, where they continue moving towards the current collector (current collector is shown red in Figure 6). Therefore the flux of electrons in thin structures of the foam especially near the current collector causes high currents and these regions have to support very high current densities ($\sim 18 \text{ A/m}^2$) which in turn depends on the structure cross section area.

During delithiation also Li-ions are detached from the LiFePO_4 and are inserted into the liquid electrolyte where they diffuse towards the Li-metal electrode. When looking Li-ion concentration gradient in the electrolyte (Figure 16b) at the end of the charging cycle then gradient is higher in the regions near the Li-metal electrode. Again this effect stays almost unchanged during the charging and shows higher rate of changing Li-ion concentrations near the Li-metal electrode. Since Li-ions are inserted into the Li-metal electrode at constant flux, the deficit of the Li-ions occurs which in turn lowers the concentration in these regions and Li-ions inserted to the electrolyte start to migrate towards the lower concentration areas (shown yellow in Figure 16b). However, liquid electrolyte have high enough diffusion coefficient and thus the magnitude of the concentration gradient is low and the flux of ions are rather uniform and homogeneous.

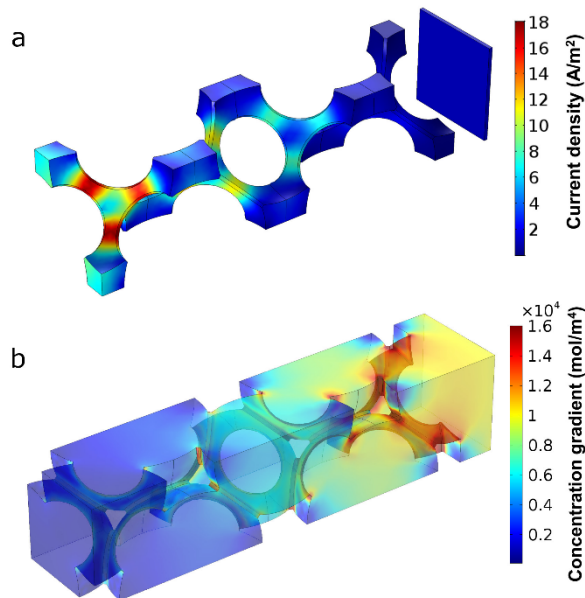


Figure 16. System snapshots at the end of the charging cycle: (a) current density (A/m^2) distribution in the carbon foam structure, (b) Li-ion concentration gradient (mol/m^4) in the electrolyte.

3.4.3 LiFePO₄ delithiation and coating homogeneity

Delithiation distribution as (x in Li _{x} FePO₄) in the 200nm thick homogeneously LiFePO₄ coated carbon foam electrode after 1500 s of charging at 3 mA/cm² (2.44 C-rate) and snapshots of the phase evolution of this electrode is presented in the Figure 17. It can be seen that delithiation reactions prefers particles near the carbon structure and these particles are almost entirely delithiated (blue) instead of particles that are closer to the electrolyte (red). Similarly, cross-section snapshots shows the progress of the delithiation which starts on the particles in the bottom of the coating layer and the electrochemical reaction evolves layer by layer in the bulk during delithiation. This behavior can be mostly caused by the very low electrical conductivity of the LiFePO₄ phase ($\sim 5 \cdot 10^{-7}$ S/m). According to the equation 1 during delithiation, electrons are detracted and inserted into carbon which acts like a high way to transport electrons towards the current collector. Therefore, LiFePO₄ particles near the carbon are preferred and this phenomena with better wiring in these regions near the current collector is also described by the Strobridge et al. [84].

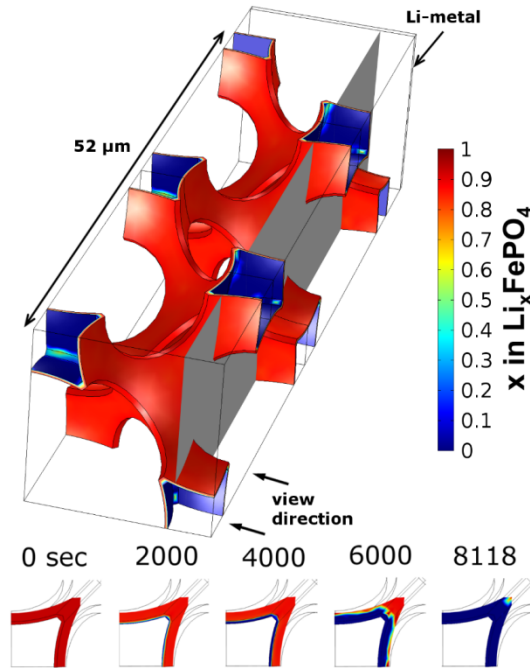


Figure 17. Depth of delithiation in the positive electrode as x in Li _{x} FePO₄ after 1500 s of charging. Gray plane show the cutoff section of the electrode and bottom row presents the snapshots of the delithiation progress of this electrode section at certain timesteps from charging the cell from 3 V up to 4 V.

Also, it is noticeable that delithiation in the LiFePO_4 evolves similarly all over the electrode, involving particles in regions near the Li-metal and also particles in region where the current is applied. This indicates rather homogeneous delithiation in this electrode which is in contrast to inhomogeneous delithiation reported previously in literature [84,85]. In that sense, present work comprises a carbon foam 3D structure with a very high electrical conductivity (100 S/m) and liquid electrolyte with the high ionic diffusivity ($3 \cdot 10^{-10} \text{ m}^2/\text{s}$). In addition, the thickness of the simulated electrode in this cell is relatively thin (52 μm) compare to the other studies (285 μm) and macropores filled with electrolyte are large ($r = 10 \mu\text{m}$). Moreover, when lower current densities are used which should render constant electrochemical reactions and therefore, most likely homogeneous delithiation develops in this system.

3.4.4 LiFePO_4 coating thickness

To investigate how the cell capacity depends on the coating thickness of the LFP in these 3D-foam cells, then five different homogeneously LiFePO_4 -coated electrodes with thicknesses of 100–500 nm were simulated. The charging voltage-capacity profiles for areal capacity (mAh/cm^2) and gravimetric capacity (mAh/g) are presented in Figure 18 a and b, respectively. It can be seen that cell footprint area capacity varies more due to the electrode mass loading than cell capacity per 1 gram of LiFePO_4 electrode material. Thicker coating therefore, clearly increases the cell capacity per footprint area from 0.59 mAh/cm^2 (100 nm coating) up to 3.09 mAh/cm^2 with the 500 nm coating, but slightly less is gained when increasing thick coatings which was expected. In another words, when volume of the LiFePO_4 increases 479 % then areal capacity rises by 424 %. The same effect can be seen in Figure 18 b when thinner coating (100 nm) shows higher gravimetric capacity (119 mAh/g) than 500 nm thick coating with slightly lower capacity of 106 mAh/g . This minor decreasing effect can be caused by the very low electrical conductivity of the LiFePO_4 and therefore according to the linear Ohm's law where thicker coatings with higher resistance causes faster cell potential rise and ohmic polarization. Still, thicker coatings are preferable in these carbon foam type systems, assuming that these are possible to achieve using current synthesis techniques. Using very thick coatings on the other hand can have decreasing effect for the cell capacity and performance, due to very long ionic diffusion pathways, high electrical resistance and clogged pores which limits the electrode/electrolyte interface area. Nevertheless, the 500 nm LiFePO_4 coating is not limiting the performance of the cell.

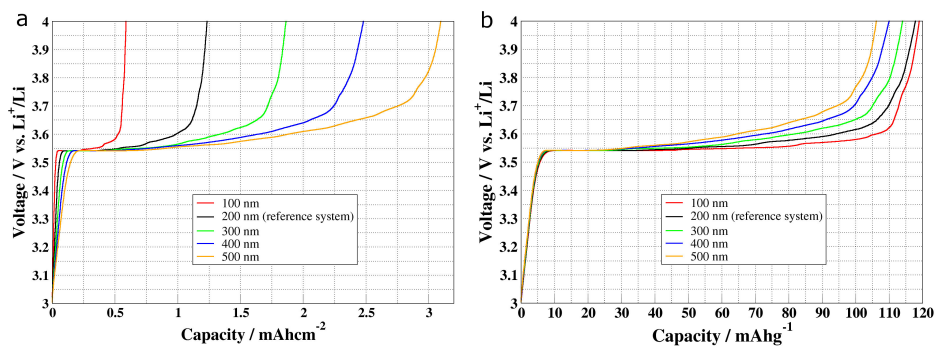


Figure 18. Voltage-capacity profiles during charging cycle of the LiFePO_4 -coated carbon foam electrode for different coating thicknesses: (a) cell capacity per footprint area (mAh/cm^2), (b) cell gravimetric capacity (mAh/g).

3.4.5 Carbon foam macropore size

Here, carbon foam macropore size is varied (average macropore radius of $5 \mu\text{m}$ and $10 \mu\text{m}$) and analyzed. Simulated cells are presented in the Figure 19 a and b, respectively. It is clear that foam with the smaller pores have more carbon material per specific volume which in turn leads to higher available coating area for LiFePO_4 particles and increased electrode mass. Since, both systems have same size of carbon area where the constant current density of $3 \text{ mA}/\text{cm}^2$ is applied then similar current flow thru the carbon structure is achieved in both system. Simulations revealed, that system with smaller macropore size and 116 % increased electrode volume obtained 111 % higher cell capacity per footprint area ($2.59 \text{ mAh}/\text{cm}^2$) compare to the system with larger macropores ($1.23 \text{ mAh}/\text{cm}^2$). While this over two times better performance per cell footprint area was expected, then such slightly less capacity gain compare to the volume increase is reasonable as explained in the previous section. Nevertheless, the simulations showed comparable gravimetric capacities of these cells and maximum current density in carbon foam remains largely the same in both systems because of the similar cross-section area of the foam structure. Moreover delithiation distribution and progress was observed to be similar and homogeneous in both systems. Li-ion concentration gradient tends to be somewhat higher in the regions near the Li-metal in the system with smaller macropores as discussed in the sections 3.4.3 and 3.4.2. Here, it can be concluded that carbon foam with the smaller macropores is the key for improving these foam type cell performances.

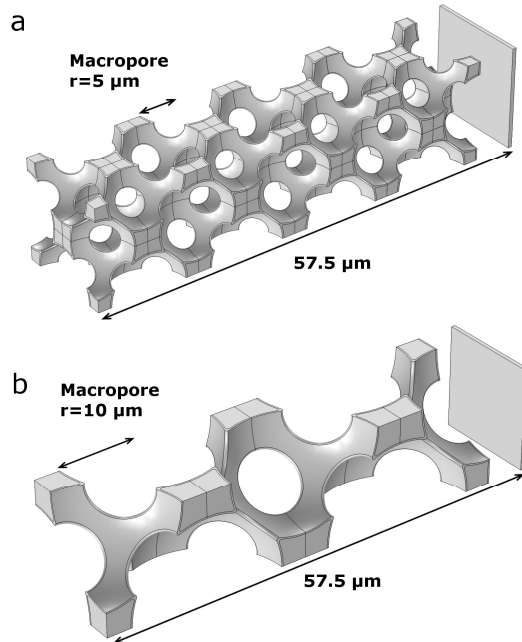


Figure 19. Simulated cell consisting LiFePO_4 -coated carbon foam with different foam macro pore sizes: (a) macropores with the radii of 5 μm , (b) macropores with radii of 10 μm .

3.5 Thermal effects in different microbattery architectures

To capture accurately the electrochemical behavior and temperature development in the MB cell the coupled multiphysics modelling has been used. This approach includes the heating calculation due to the cell electrochemistry and mass transportation. Also temperature dependences on the properties of ionic transportation and electrochemical kinetics has been taken into account. Therefore this model have more precise description of natural phenomena occurring in the Li-ion cell and makes these FEM simulations to a viable tool for highlighting the overheating regions, developing 3D electrode designs and comparing different 3D cell architectures.

The temperature behavior of some proposed 3D architectures at discharge current densities (1 and 10 A/m^2) are presented in the Figure 20. It has to be mentioned that these temperature profiles during cell discharging are typical for LCO/graphite cells and are comparable with the results showed in literature [68,86]. Simulations shows the tendency that higher current density (10 A/m^2) increases the average temperature (15 $^\circ\text{C}$) in the interdigitated and concentric cell and lower current density (1 A/m^2) rises temperature 13 $^\circ\text{C}$ in these cells. This tendency exist due to the irreversible Joule heating (Equation 27) and reversible heat generation mechanism caused by the electrochemical reactions

according to the equation 26 as expected. Therefore, thermal behavior (Figure 20 a and b) is similar in the interdigitated and concentric architecture but somewhat differs in the trench cell. The simulation duration is almost 2 times shorter and also temperature rise is twice as fast in the trench cell compare to the other architectures at all discharge rates. Moreover, trench architecture presents also highest average temperature at the end of the simulation which is approximately 5 °C higher than temperature in other cells. This phenomena indicates the imbalance of electrodes material or ineffective electrode material utilization in this architecture. This effect can be caused by the inhomogeneous current densities and undesired high local electrochemical behavior.

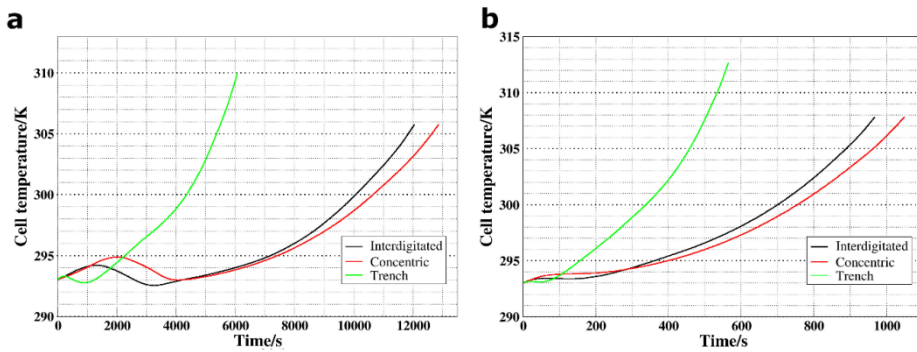


Figure 20. Thermal profiles of the interdigitated, concentric and trench architectures at various discharge current densities: (a) 1 A/m², (b) 10 A/m².

Another interesting effect occurs in all the systems at the first third of the total discharge cycle especially when lower current densities are used. It can be seen that average cell temperature at some point starts to decrease and then rise again. This so called “cooling down effect” is caused by the thermochemistry of the electrochemical reactions arising especially in the LiCoO₂ electrode and is therefore very characteristic for this electrode material [65,68,87,88]. Thermochemistry of the LiCoO₂ depends on the state of charge in terms of intercalation of the lithium ions into the crystal structure [89]. During cell discharge cycle, when LiCoO₂ is lithiated the reaction is partially endothermic in the range $0.57 < x < 0.64$ as stated in the literature [88]. While the overall heat in the cell during discharging can be generated by the internal resistance and delithiation of the graphite, the energy can be consumed during LiCoO₂ delithiation. The interplay between these sources and sinks may cause the average decline of the cell temperature, since the endothermic processes during certain phase will dominate.

Moreover reversible and irreversible heat sources in these Li-ion MBs at constant current densities 10 A/m² are separately presented in the Figure 21 to get more detailed insights about cell thermal behavior. Reversible heating in the

cell is caused by the electrochemical reactions and irreversible heating is heat generated due to the electronic and ionic resistances of the electrode and electrolyte materials. It is visible that reversible heating is almost orders of magnitude higher and have therefore major impact for cell temperature rise. Also reversible heating in the positive electrode dominates over the negative electrode and therefore sudden heating decline in the positive electrode (Figure 21 a, solid lines) at the beginning of the discharge explains the cause of temperature decrease as “cooling down effect” in the cell. It has to be mentioned that the overall magnitude and rang of the entropy for LiCoO_2 is substantially higher than other positive electrode materials (LiMn_2O_4 , LiFePO_4 and $\text{Li}_{4/3}\text{Ti}_{5/3}\text{O}_4$) indicating that heat generation can be highly decisive and depends vastly on state of charge in the LiCoO_2 electrode [89,90]. Thus, the reversible heat produced by the positive electrode has major impact even if the irreversible heat generated due to the cell resistance and ohmic losses is somewhat higher in the negative electrode.

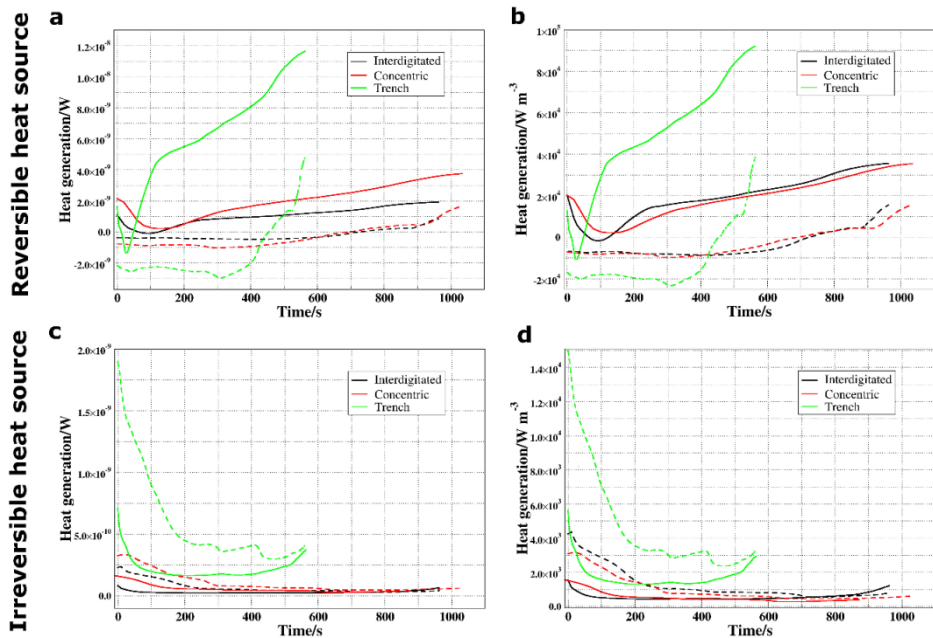


Figure 21. Heat generation in three different Li-ion MBs during discharging under current density of 10 A/m^2 . Reversible heat sources: (a) Total heat generation, (b) Volumetric heat generation W/m^3 and irreversible heat sources: (c) Total heat generation, (d) Volumetric heat generation W/m^3 . Solid lines represent positive electrode (LiCoO_2) and dotted line negative electrode (graphite), respectively.

Volume normalized heat generation (Figure 21 b and d) shows that concentric architecture demonstrates the lowest overall heat generation (W/m^3) in both heat source terms. In contrast heat generation by both source types is notably higher in the trench architecture compare to the other geometries. This difference should be caused by the geometrical aspects and certain configuration of the electrodes in trench design. Therefore, wide walls of the positive electrode includes correspondingly larger current collectors and which possibly provide much higher local current densities and thereby increases electrochemical activity.

Since these used materials have high heat transfer coefficient in the context that discharging time is relatively long and dimensions are in the microscale which lead to the rather uniform temperature distribution. Temperature gradient on the other hand can be used to highlight temperature changes and critical heat sources in the cell. Therefore, to have more detailed explanation behind somewhat different behavior of the trench architecture, the snapshots of temperature gradient in all the cell types during the discharge cycle at constant current density ($10 \text{ A}/\text{m}^2$) are plotted in the Figure 22. It can be seen that temperature gradient is higher in the regions near the tips of the LiCoO_2 electrode which can lead to the higher heating and electrochemical activity in the pillars/plates rather than in the base layer which in turn leads to the similar conclusion as discussed previously in the sections 3.1 and 3.3.1. However, one exception occurs near the 3.9 V where the temperature gradient is smallest during the discharge cycle. This is related with the so called “cool down effect” which is in a good agreement with the previous discussion.

Highest heat generation observed in the trench cell can be also confirmed by the last row of Figure 22, especially at the second half of the discharge cycle. Temperature gradient highlights the regions where the most active charge transfer processes takes place. This inhomogeneous electrochemical activity and therefore locally high heat sources can be caused by the geometrical aspects of this architecture. The wide plate tips of the LiCoO_2 electrodes consists also wide current collectors which in turn are very close to the opposing negative electrode and the distance is relatively short between these opposing current collectors. Therefore, this correspond to the areas with lowest resistance which provides high electric field and inhomogeneous current density distribution in the cell. Thereby this undesired high local currents in turn generates more heat and rises temperature which affect the electrolyte and electrode material parameters. Since the rising temperature increases the conductivity and ionic diffusivity of the polymer electrolyte (equations 29, 30 and 31) and resistance of the electrolyte and electrodes decreases, the possibly quicker electrochemical reactions can be occurred. In addition, according to the (equation 31) electrochemical kinetics are also enhance exponentially with the temperature rise, which in turn, result in a higher heat generation and again further temperature increase. This locally high heat sources in the certain regions induces large temperature fluctuations and put unbalanced stress on the cell. Hereafter, this can seriously affect overall cell performance, lifetime and can lead to safety hazards which sets an upper operating temperature limit for the battery.

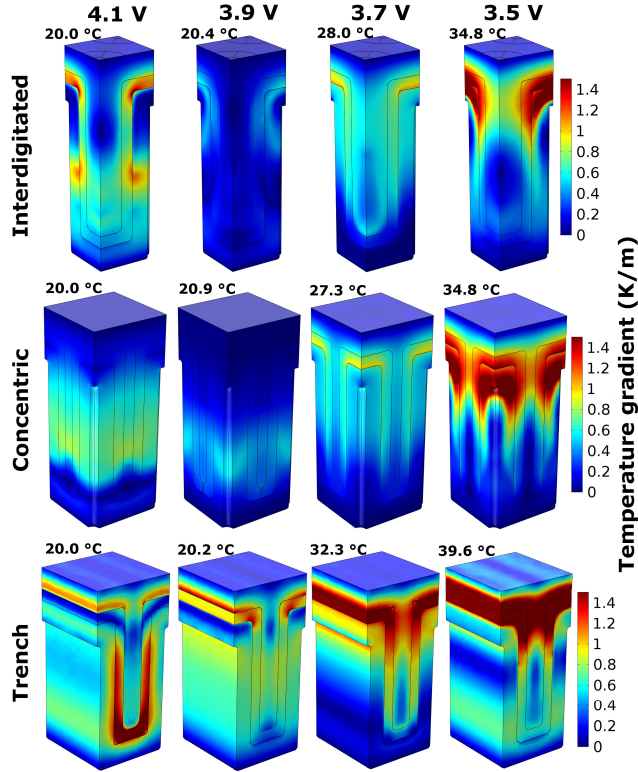


Figure 22. Snapshots of temperature gradient development in 3D-MBs with different architectures at certain cell voltages during discharging with constant current density of 10 A/m^2 .

3.6 Designing 3D microbatteries

3.6.1 Polymer electrolyte vs. liquid electrolyte

Designing battery cells comprises also with choice of using best suitable materials. Therefore, the effect of electrolyte diffusion coefficient on the temperature and cell performance is also studied. Three different cell architectures using liquid electrolyte – 1.5 M LiPF_6 in ethylene carbonate : dimethyl carbonate (1:2 by volume) are compared with the systems with polymer electrolyte – 1.5 M LiTFSI in poly(ethylene oxide). Modelled liquid electrolyte (Equation 29) exhibit higher diffusion coefficient ($D \approx 10^{-9} \text{ m}^2/\text{s}$) and polymer electrode (Equation 30) provides lower diffusion coefficient of ($D \approx 10^{-12} \text{ m}^2/\text{s}$) under constant discharge current density of 4 A/m^2 . Other thermal properties can be find in the paper II.

Cells discharge curves are presented in the Figure 23 a in terms of gravimetric capacity (mAh/g). Simulations show that higher ionic diffusivity in the electrolyte increases the cell capacity about 18% in the concentric, 25% in the interdigitated and 44% in the trench architecture. The cell capacity differences between these systems as discussed previously (section 3.5) more or less dis-

appear. Therefore, higher ionic diffusivity in the electrolyte will reduce one of the transportation bottlenecks in the Li-ion MBs and increases available capacity of the cell.

The average temperature in the different cell geometries with varied electrolytes are plotted in the Figure 23 b. It can be seen that at the end of the discharge cycle, the average cell temperature is 2 °C lower in the systems using liquid electrolyte than in the systems with polymer electrolyte. This better thermal behavior is due to the higher ionic diffusivity in the electrolyte, which leads to reduced internal resistivity and therefore lower heat generation. Here one can conclude, that material properties and thereby thickness of the electrolyte has major impact to the battery performance and thermal behavior. However, use of liquid electrolyte is more complicated or nearly even impossible to practically use in such complex MB architectures due to the lack of mechanical support to separate the electrodes. Thus, solid or polymer electrolytes with the high ionic diffusivity is desired in these MBs.

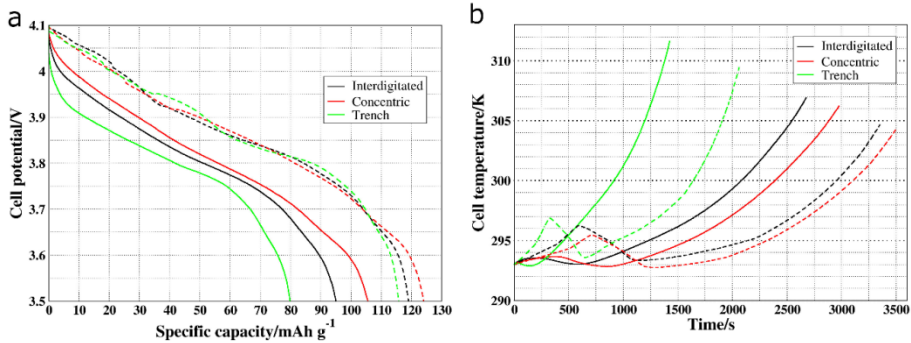


Figure 23. Discharge cycle of different 3D-MB geometries at constant current density of 4 A/m²: a) cell voltage profiles, b) average cell temperature development. Solid lines presents the polymer electrolyte and dotted lines shows liquid electrolyte.

3.6.2 Electrode material rearrangement in the concentric architecture

This study evolves the electrode material arrangement order in the Li-ion MB with concentric architecture Figure 3c. Thus, which electrode on top provides the best cell performance: anode on cathode vs. cathode on anode. In this particular architecture (pillar height of 60 μm and interpillar distance of 12 μm, Figure 24 c and d) the volume of the pillared electrode is 1.4 times smaller than the volume of the opposite electrode which gives different electrode material loadings. On the other hand volumetric energy density for LiCoO₂ is ~1.6 times lower than that of LiC₆ and therefore material selection for each electrode becomes essential for effective battery energy density usage. In Figure 24 c and d both material configurations are presented where reference system comprises

LiCoO₂ for positive pillared electrode coated with electrolyte and filled with graphite.

The discharge curves and lithiation level in Li_xCoO₂ of these systems under various current densities are displayed in Figure 24 a and b, respectively. It can be seen that discharge duration is longer in the reverse system, therefore larger volume of the positive electrode increases the cell discharge time up to factor of 2 if lower current density (1 A/m²) was used which in turn indicates increased energy. However, difference between discharge duration in these systems is less significant when higher current densities (4 and 8 A/m²) are used. This behavior can be caused by the different electrical conductivities of the electrode materials where graphite has significantly higher conductivity than LiCoO₂ (10 vs 0.01 S/m). Therefore in reference design current collectors improve the electronic flow in to the LiCoO₂ pillars and this in turn favors a development of much deeper average delithiation level at the end of the charging cycle (at the beginning of the discharge cycle) as seen in the Figure 24 b under all current densities.

In addition, snapshots of the lithiation distribution of the Li_xCoO₂ electrode after 1600 s of discharging the cell using current density of 4 A/m² in both design is presented in Figure 24 c and d. It can be seen that high enough electrical conductivity of the graphite counter electrode in reference system also provides a more homogeneous lithiation/delithiation of the LiCoO₂ electrode. Reversed design with high conductivity graphite pillars on the other hand will therefore pass the current thru the tips of the pillars and degree of lithiation of the opposite LiCoO₂ electrode is higher in the regions near the graphite pillar tips (Figure 24 d). This leads to the non-uniform lithiation, concentration polarization and underutilized regions of the LiCoO₂ electrode in the reversed design. This ineffective material usage of the LiCoO₂ material is also seen from the narrow range of the average value for depth of delithiation, seen in the Figure 24 b ($0.81 < x < 0.94$ in Li_xCoO₂ for 8 A/m²). Thus, reversed design – cathode on anode – with large amount of stored positive electrode material provides high energy density when low current density is used, while a significantly deeper and more homogeneous positive electrode delithiation can be achieved with the reference – anode on cathode – design.

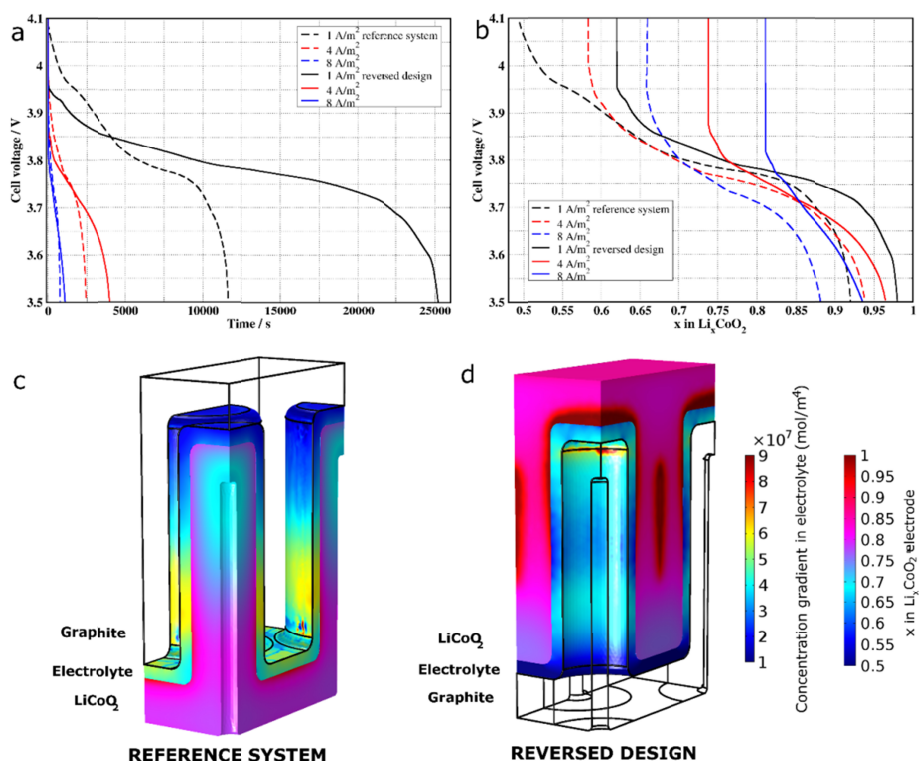


Figure 24. Comparison of reference system and design with reversed order of electrode materials: (a) Discharge profiles of the cells, (b) Lithiation level in the positive electrode (Li_xCoO_2), (c) and (d) Lithiation distribution in the positive electrode and concentration gradient in the electrolyte after 1600s of discharging for a current density of 4 A/m^2 .

3.6.3 Comparison of 3D MB architectures

Comparing all four proposed architectures in these studies gives good evaluation and puts these cell designs into perspective. In table 1 theoretically usable electrode capacity and gravimetric capacity of these four different designs under the current density of 10 A/m^2 are presented. Therefore, LiFePO_4 with 124 % higher reversible capacity in the foam type 3D electrode architecture shows 148 % higher capacity per gram of positive electrode compared to the concentric architecture with the LiCoO_2 electrode. It has to be mentioned that when trench, interdigitated and concentric designs were full cell systems then here foam type 3D electrode was simulated as a half-cell. Therefore, the limiting part of the battery processes by the negative electrode is not taken into account and somewhat higher results were expected. For more accurate comparison, the full cell consisting of foam type electrode should be developed and characterized. Still these simulations show that highest performance can be achieved with the concentric

architecture and that LiFePO₄-coated carbon foam as an electrode in 3D micro-batteries has promising designing idea.

Table 1: Comparison of four different simulated 3D Li-ion microbatteri architectures.

	Positive electrode material	Discharge current density / Am⁻²	Theoretical reversible capacity / mAhg⁻¹	Calculated capacity / mAhg⁻¹
Trench	LiCoO ₂	10	137	80
Interdigitated	LiCoO ₂	10	137	86
Concentric	LiCoO ₂	10	137	93
Foam	LiFePO ₄	10	170	138

4 CONCLUSION AND OUTLOOK

In this theses, computer simulations of various 3D Li-ion microbattery architectures has been performed in the context of designing and optimizing the cell architecture and geometry of electrodes for improving battery energy capacity and performance via Finite Element Method. This work has provided new insights into the mass transportation phenomena occurring in these different proposed cell concepts and parametric studies suggests the optimal electrode geometrical dimensions to increase cell capacity and design cells with most homogeneous electrochemical activity. Another major contribution was developing and simulating fully coupled 3D thermal-electrochemical Li-ion battery model to predict temperature development and temperature, which in turn, influences the dynamics of electrochemical processes and materials transport properties. In addition, aperiodic 3D Li-ion MB model was successfully experimentally validated and various parametric simulations was carried out. Hereby, interdigitated, concentric, trench and aperiodic 3D-architectures are constructed, one full charge/discharge cycle is modelled and investigated.

Parametric simulations of the 3D concentric microbattery consisting of LiCoO_2 pillared electrode coated with polymer electrolyte and graphite counter electrode demonstrated the pillar length and interpillar distance impact to the cell performance. Expected cell design would provide both high capacity and most homogeneous electrochemical activity over the entire electrode surface area to achieve most efficient cell volume usage. Higher pillars with more electrode material increases the cell capacity per footprint area while depth of delithiation of the LCO decreases which results in a higher proportion of inactive material. Since pillars are more active than the electrode base layer due to the ionic diffusion distance to the opposing electrode, then lower pillars show deeper but more inhomogeneous delithiation. Interpillar distance variation on the other hand suggests closer pillars which increases electrode material loading and thus capacity per cell footprint area. However optimal concentric 3D microbattery geometry comprises pillar heights of $70\ \mu\text{m}$ and interpillar distances of $10\ \mu\text{m}$ where high cell capacity and homogeneous lithiation are both achieved.

Another set of experimentally calibrated parametric simulations of electrochemical system containing a nanosized LiFePO_4 -coated carbon foam electrode revealed that lower current density ($0.1\ \text{mA}/\text{cm}^2$) increases 36 % of the cell capacity (mAh/g) compare to high current density ($3\ \text{mA}/\text{cm}^2$). It was noted that delithiation is very homogeneous in this foam type electrodes and electrochemical reactions prefers particles near to the carbon foam structure. These effects are caused by the characteristically very low electrical conductivity ($\sim 1 \cdot 10^{-7}\ \text{S}/\text{m}$) of the LiFePO_4 where during delithiation Li-ions are inserted into the electrolyte where they diffuse towards opposing electrode and electrons are inserted into the electrically high conducting carbon structure where they move towards the current collector. In experimental point of view most promising performance of the cell with foam type electrode should be achieved when the smaller macro-

pores are used. This increases the available electrode coating area and together with thick coating the material loading is increased and cell capacity per footprint area is enhanced. Generally, this shows that porous carbon structure can be an excellent template for the LiFePO_4 coating and this in turn improves global electronic and ionic access. Moreover, rate performance of this cell depends strongly on the structure of the composite electrode. Therefore, practical 3D Li-ion MB performance can be improved using this novel foam type electrodes, however synthesizing these composite foam type electrodes with small uniform macropores and thick electrode loadings can be a difficult challenge for experimentalists.

More advanced thermal and electrochemical coupled Li-ion battery model showed that performance in terms of capacity and heat generation in the proposed MB architectures depends widely on the charging/discharging rates. Cell capacities decrease approximately 20% when 10 times higher current density (10 A/m^2) was used. Since, ionic transportation and electrochemical activity follows exponential Arrhenius type relation, thus rapid temperature development can be observed especially in the trench architecture. Latter cell geometry has wide positive electrode current collectors near the opposite current collector plate and this design generates high local current densities and therefore high electrochemical activity and in turn temperature rise increases the charge transfer processes in these regions. These critical areas in the cell can be highlighted via temperature gradient and this most likely leads to the bottlenecks of the electrodes design and safety hazards. Highest performance and lowest cell temperatures at all charge rates were noticed to be in the 3D-MB with the concentric architecture. Simulations also showed that more diffusive electrolyte (i.e. liquid electrolyte) instead of polymer electrolytes in these systems provide over 20 % higher capacity and heat generation can be significantly mitigated. Therefore, thermal simulations are very useful tool for understanding heat generation in the batteries, highlighting heat sources and electrochemically most active regions and thus are suitable for optimization of the cell geometry in terms of both safety and performance.

Notably, electrodes energy balance is crucial for designing MB cell with maximum energy density then theoretical and practical energy density of the electrodes material has to be considered. It has been showed with the simulation that there is a major difference for example in the concentric designs if the LCO or graphite is used as a pillared electrode due to the differences in electrode volume. Since graphite has 1.6 times higher energy density than practical energy density of LCO then smaller volume (pillared electrode) for negative electrode provides better energy balance in the cell and discharge time was almost two times longer when lower discharge rates are used. However, this design renders more nonhomogeneous electrochemical activity over the electrodes surfaces and therefore higher rates are not suggested and possible loss of power density can be notice.

Nevertheless, this electrode material rearrangement effects with various electrolyte and electrode transportation parameters should be studied further in

future. In Practical point of view it could be argued that pillared graphite electrode coated with polymer electrolyte and this in turn is filled up with the LCO electrode material is more difficult to fabricate than thin-film oxide on the current collector. Also current collector aspect as a highway for electrons for low electrically conductive electrode (i.e LiCoO_2 or LiFePO_4) material should be deeper investigated. Similarly, interdigitated architecture where both pillared electrodes have different pillar arrangements or ratios to achieve better energy balance in the cell, has to be studied.

Moreover, to develop further this present thermal-electrochemical 3D-MB model then physical electrode expansion should also be implemented to take account the material dimension changes due to the lithiation/delithiation. Thus, this improved Li-ion MB model should highlight also critical areas and imbalances because of the inner forces in the materials. This helps to understand further the electrochemical behavior and mass transportation phenomena in these cells.

It also should be mention that in theory there is many MB designing ideas and concepts which can be computationally built, study and design, but it is relatively difficult to develop the material synthesis and fabrication techniques and assemble experimentally these hypothetical cells. Therefore, computer simulations should help experimentalists to choose more promising material combinations and optimal geometrical configurations and dimensions for most promising Li-ion MB cells in terms of energy capacity and safety under high charge/discharge rates.

5 SUMMARY IN ESTONIAN

3D mikroakude arendamine ja optimeerimine

Elektronika ja kaasaskantavate seadmete areng on tänapäeval ülikiire, nende mõttmed järjest enam vähenevad ja energia tarve suureneb. Näiteks elektromehaanilised mikrosüsteemid vajavad energiaallikaid, mis on samuti oma mõtmetelt mikro skaalas ning omavad suurt võimsustihedust ning suudavad salvestada piisaval hulgal energiat. Üks võimalikke viise mikroakude energiatihedust tõsta on kasutada 3-mõõtmelist Liitium-ioon aku arhitektuuri. Varasemad uuringud on näidanud, et just selliste 3-mõõtmeliste elektrootide pindala on märkimisväärselt suurem, mistõttu on võimalik kasutada suuremaid laadimis ja tühjakslaadimis voolusid ja selliste akude võimsustihedus kasvab. Samuti saab 3-mõõtmeliste elektrootide puhul kasutada rohkem elektrooti materjali raku pindalaühiku kohta, mis omakorda tõstab aku energiatihedust. Seega antud arhitektuuri korral võiks aku energiatihedus kasvada 10 korda võrreldes tavapärase Liitium-ioon akuga, kus kasutatakse planaarseid elektrootde. 3-mõõtmelised akud on siiski veel arendusjärgus ja siinkohal ongi arvutisimulatsioonid ja akumodelite disainimine suureks abiks eksperimentalistidele, et välja töötada ja optimeerida elektrootide struktuure, saavutamaks teoreetiliselt parimaid tulemusi.

Antud doktoritöö väljund on meetodika arendamine ja simulatsioonides kasutatavate mudelite loomine ning modelleerimine. Eesmärgiga leida Liitium-ioon mikroakude elektrootide struktuur, mis annab suurima mahtuvuse ja ühtlase elektrokeemilise aktiivsuse ning laengutiheduse jaotuse elektrootide pindadel, kasutades lõplike elementide meetodit programmiga *COMSOL Multiphysics*. Selline lähenemine annab võimaluse parameetriselt muuta mudelite geomeetriasi mõõtmeid ja lihtsasti muuta aku mudelis kasutatavate materjalide omadusi.

Käesolevas töös on uuritud 4 erinevat 3D Liitium-ioon mikroaku arhitektuuri, et kirjeldada täpsemalt nendes keerulistes süsteemides toimuvat massitransporti ning võrrelda akude temperatuuri jaotust ja mahtuvust. Temperatuurist sõltuvad elektrokeemilised simulatsioonid toovad hästi esile elektrootide elektrokeemiliselt aktiivsed piirkonnad ja temperatuuri gradiendid määravad ära elektrootide soojust tootvad ja neelavad alad. Selliselt on võimalik kindlaks teha nende eri tüüpi arhitektuuride massi transporti piiravad piirkonnad ning jälgida temperatuuri kasvu eri piirkondades aku laadimisel ja tühjaks laadimisel. Simulatsioonid näidavad, et concentric Liitium-ioon mikroaku arhitektuuri kasutades on võimalik saavutada maksimaalne energiatihedus 93 mAh/g positiivse elektrooti grammi kohta. Interdigitated ja trench arhitektuur näitasid vastavalt 86 ja 80 mAh/g mahtuvust. Väikseima mahtuvusega trench süsteemi korral täheldati ka kõige suuremat temperatuuri kasvu, mis viitab antud elektrootide konfiguratsioonist tulenevatele kitsaskohtadele. Suurima mahtuvusega concentric süsteemi täiendavad parameetriselised simulatsioonid näitasid, et lühemate sammaste (40 μm) korral on LiCoO_2 positiivsest elektrootist võimalik kätte saada rohkem liitium ioone ning seega aktiivaine kasutamine on tõhusam. Kõrgemad sambad (100 μm) aga näitasid suuremat energia tihedust aku pindala kohta, kuid piiratud kogu

elektroodi materjali kasutamist. Seetõttu võiks optimaalseks samba kõrguseks lugeda 70 μm ja sammaste vahekauguseks 12 μm , et saavutada akus parim energia ja ruumala suhe.

Lisaks koostati Uppsala ülikool eksperimentaalsete tulemuste põhjal kalibreeritud akumudel uudsest 3D mitteperioodilisest vaht-tüüpi komposiitelektroodist. Parameetrilised simulatsioonid näitasid, et madalamad volutihedused, väiksemad makropoorid ja paksemad elektroodmaterjali kattekihid pakuvad suuremat energia tihedust aku pindala kohta ning isegi 500 nm paksuse elektroodi kihi korral ei märgatud limiteerivaid tegureid. Täheldati, et elektrokeemiline aktiivsus oli väga homogeenne ja reaktsioonid eelistavad LiFePO_4 nanoosakesi mis on süsinik-vaht elektroodi pinna vahetus läheduses.

Kokkuvõttes võib öelda, et sellised elektrokeemilised simulatsioonid Liitiumioon mikroakudest on väga kasulikud tööriistad nende arhitektuuri arendamiseks ja elektroodide disainimiseks. Nii on võimalik kergesti muuta elektroodi ja elektrolüüdi geomeetrisi mõõtmeid ja materjalide fundamentaalseid parameetreid, et leida optimaalsed mõõtmed, mille korral aku mahtuvus ja vastupidavus on suurimad. Siiski tuleb ära märkida, et teoreetiliselt on arvutis akumodelite koostamine ja disainimine suhteliselt lihtsustatud, kuid eksperimentaalselt selliste kompleksete elektroodi struktuuridega aku koostamine on keeruline, mistõttu tuleb edasi arendada mikro skaalas Liitium-ioon akude monteerimise ja tootmise tehnikat ning materjalide sünteesi meetodeid.

6 ACKNOWLEDGEMENTS

First I would like to thank my professor Alvo Aabloo who gave me this opportunity and supported me throughout this study. I would also like to thank my main supervisor Vahur Zadin for all the open discussions about every aspect of Li-ion batteries and simulations. Also I would like to acknowledge my supervisor Heiki Kasemägi who helped me develop a curious and critical mind and helped me with the administrative duties. Special thanks goes for professor Daniel Brandell for numerous discussions about electrochemistry and who host me during the visit of Battery Group in Ångström laboratory.

This research was supported by the Estonian Research Council Grant PUT 57, PUT 1372 and Estonian Science Foundation Grant ETF9216. This work has been also partially supported by Graduate School of Functional materials and technologies receiving funding from the European Regional Development Fund in University of Tartu, Estonia.

All the colleagues at IMS lab, thank you for making this journey especially enjoyable!

I also want to thank my family and friends who have supported me through it all!

Thank you!

7 APPENDIX

Table 2. Parameters used in thermal simulations

Symbol	Name/description	Value	Unit	Ref.
A	Electrolyte pre-exponential factor	$1 \cdot 10^{-6}$	$\text{K}^{0.5} \text{m}^2/\text{s}$	[73]
E_a	Electrolyte activation energy	0.38	eV	[73]
T_g	Electrolyte glass transition temperature	-40.1	$^{\circ}\text{C}$	[91]
$D_{0,a}$	Initial solid-state diffusion (graphite)	$2 \cdot 10^{-12}$	m^2/s	[70]
$D_{0,c}$	Initial solid-state diffusion (LiCoO_2)	$1 \cdot 10^{-11}$	m^2/s	[92]
$k_{0,a}, k_{0,c}$	Initial reaction rate (graphite, LiCoO_2)	$2 \cdot 10^{-11}$	m/s	[57,62]
Ea_{Da}	Diffusivity activation energy (graphite)	1663	J/mol	[93]
Ea_{Dc}	Diffusivity activation energy (LiCoO_2)	7483	J/mol	[93]
Ea_{ka}	Reaction rate activation energy (graphite)	14965	J/mol	[93]
Ea_{kc}	Reaction rate activation energy (LiCoO_2)	14965	J/mol	[93]

8 REFERENCES

- [1] Key world energy statistics – International Energy Agency, 2016.
- [2] F. Chamran, H. Min, B. Dunn, C.C.J. Kim, Zinc-Air microbattery with electrode array of Zinc microposts, *MEMS*. (2007) 871–874.
- [3] Y. Wu, *Lithium-Ion Batteries Fundamentals and Applications*, London, 2015.
- [4] J.F. Rohan, M. Hasan, S. Patil, D.P. Casey, T. Clancy, Energy Storage : Battery Materials and Architectures at the Nanoscale, *ICT – Energy – Concepts Towar. Zero – Power Inf. Commun. Technol.* (2014) 107–138. doi:10.5772/57139. Available.
- [5] W.A. van Schalkwijk, B. Scrosati, *Advances in Lithium-Ion Batteries*, Springer US, Boston, MA, 2002. doi:10.1007/b113788.
- [6] J.M. Tarascon, M. Armand, Issues and challenges facing rechargeable lithium batteries., *Nature*. 414 (2001) 359–367.
- [7] T. Ohzuku, R.J. Brodd, An overview of positive-electrode materials for advanced lithium-ion batteries, *J. Power Sources*. 174 (2007) 449–456. doi:10.1016/j.jpowsour.2007.06.154.
- [8] J.H. Pikul, P. V. Braun, W.P. King, Performance Modeling and Design of Ultra-High Power Microbatteries, *J. Electrochem. Soc.* 164 (2017) E3122–E3131. doi:10.1149/2.0151711jes.
- [9] L.O. Valoén, J.N. Reimers, Transport Properties of LiPF₆-Based Li-Ion Battery Electrolytes, *J. Electrochem. Soc.* 152 (2005) A882. doi:10.1149/1.1872737.
- [10] M. Kotobuki, Y. Suzuki, H. Munakata, K. Kanamura, Y. Sato, K. Yamamoto, et al., Effect of sol composition on solid electrode/solid electrolyte interface for all-solid-state lithium ion battery, *Electrochim. Acta*. 56 (2011) 1023–1029. doi:10.1016/j.electacta.2010.11.008.
- [11] L. Edman, M.M. Doeff, A. Ferry, J. Kerr, L.C. De Jonghe, Transport Properties of the Solid Polymer Electrolyte System P(EO)_n LiTFSI, *J. Phys. Chem. B*. 104 (2000) 3476–3480.
- [12] Y. Wang, W.D. Richards, S.P. Ong, L.J. Miara, J.C. Kim, Design principles for solid-state lithium superionic conductors, *Nat. Mater.* 14 (2015) 1026–1032. doi:10.1038/NMAT4369.
- [13] S. Holmberg, A. Perebikovskiy, L. Kulinsky, M. Madou, 3-D Micro and Nano Technologies for Improvements in Electrochemical Power Devices, *Micro-machines*. 5 (2014) 171–203. doi:10.3390/mi5020171.
- [14] W. Wu, X. Xiao, X. Huang, The effect of battery design parameters on heat generation and utilization in a Li-ion cell, *Electrochim. Acta*. 83 (2012) 227–240. doi:10.1016/j.electacta.2012.07.081.
- [15] D. Golodnitsky, M. Nathan, V. Yufit, E. Strauss, K. Freedman, L. Burstein, et al., Progress in three-dimensional (3D) Li-ion microbatteries, *Solid State Ionics*. 177 (2006) 2811–2819. doi:10.1016/j.ssi.2006.02.048.
- [16] J.F.M. Oudenhoven, L. Baggetto, P.H.L. Notten, All-Solid-State Lithium-Ion Microbatteries: A Review of Various Three-Dimensional Concepts, *Adv. Energy Mater.* 1 (2011) 10–33. doi:10.1002/aenm.201000002.
- [17] F. Albano, M.D. Chung, D. Blaauw, D.M. Sylvester, K.D. Wise, A.M. Sastry, Design of an implantable power supply for an intraocular sensor, using POWER (power optimization for wireless energy requirements), *J. Power Sources*. 170 (2007) 216–224. doi:10.1016/j.jpowsour.2007.04.007.

- [18] M. Roberts, P. Johns, J. Owen, D. Brandell, K. Edstrom, G. El Enany, et al., 3D lithium ion batteries – from fundamentals to fabrication, *J. Mater. Chem.* 21 (2011) 9876–9890. doi:10.1039/c0jm04396f.
- [19] J.W. Long, B. Dunn, D.R. Rolison, H.S. White, Three-dimensional battery architectures., *Chem. Rev.* 104 (2004) 4463–4492. doi:10.1021/cr020740l.
- [20] P.L. Taberna, S. Mitra, P. Poizot, P. Simon, J.M. Tarascon, High rate capabilities Fe₃O₄-based Cu nano-architected electrodes for lithium-ion battery applications, *Nat. Mater.* 5 (2006) 567–573. doi:10.1038/nmat1672.
- [21] J.M. Haag, G. Pattanaik, M.F. Durstock, Nanostructured 3D electrode architectures for high-rate Li-ion batteries, *Adv. Mater.* 25 (2013) 3238–3243. doi:10.1002/adma.201205079.
- [22] D. Golodnitsky, V. Yufit, M. Nathan, I. Shechtman, T. Ripenbein, E. Strauss, et al., Advanced materials for the 3D microbattery, *J. Power Sources.* 153 (2006) 281–287. doi:10.1016/j.jpowsour.2005.05.029.
- [23] S.K. Cheah, E. Perre, M. Rooth, M. Fondell, A. Hårsta, L. Nyholm, et al., Self-Supported three-dimensional nanoelectrodes for microbattery applications, *Nano Lett.* 9 (2009) 3230–3233. doi:10.1021/nl9014843.
- [24] T.S. Arthur, D.J. Bates, N. Cirigliano, D.C. Johnson, P. Malati, J.M. Mosby, et al., Three-dimensional electrodes and battery architectures, *MRS Bull.* 36 (2011) 523–531. doi:10.1557/mrs.2011.156.
- [25] H. Ning, J.H. Pikul, R. Zhang, X. Li, S. Xu, J. Wang, et al., Holographic patterning of high-performance on-chip 3D lithium-ion microbatteries, *Proc. Natl. Acad. Sci.* 112 (2015) 6573–6578. doi:10.1073/pnas.1423889112.
- [26] R.W. Hart, H.S. White, B. Dunn, D.R. Rolison, 3-D Microbatteries, *Electrochem. Commun.* 5 (2003) 120–123. doi:10.1016/S1388-2481(02)00556-8.
- [27] F. Chamran, Y. Yeh, H. Min, B. Dunn, C. Kim, Fabrication of High-Aspect-Ratio Electrode Arrays for Three-Dimensional Microbatteries, *Microelectromechanical Syst.* 16 (2007) 844–852.
- [28] K. Sun, T.-S. Wei, B.Y. Ahn, J.Y. Seo, S.J. Dillon, J. a Lewis, 3D printing of interdigitated Li-ion microbattery architectures., *Adv. Mater.* 25 (2013) 4539–4543. doi:10.1002/adma.201301036.
- [29] J.H. Pikul, H. Gang Zhang, J. Cho, P. V Braun, W.P. King, High-power lithium ion microbatteries from interdigitated three-dimensional bicontinuous nanoporous electrodes., *Nat. Commun.* 4 (2013) 1732–1736. doi:10.1038/ncomms2747.
- [30] G. Oltean, L. Nyholm, K. Edström, Galvanostatic electrodeposition of aluminium nano-rods for Li-ion three-dimensional micro-battery current collectors, *Electrochim. Acta.* 56 (2011) 3203–3208. doi:10.1016/j.electacta.2011.01.053.
- [31] L. Baggetto, R.A.H. Niessen, F. Roozeboom, P.H.L. Notten, High energy density all-solid-state batteries: A challenging concept towards 3D integration, *Adv. Funct. Mater.* 18 (2008) 1057–1066. doi:10.1002/adfm.200701245.
- [32] P.H.L. Notten, F. Roozeboom, R. a. H. Niessen, L. Baggetto, 3-D Integrated All-Solid-State Rechargeable Batteries, *Adv. Mater.* 19 (2007) 4564–4567. doi:10.1002/adma.200702398.
- [33] J. Xie, J.F.M. Oudenhoven, D. Li, C. Chen, R. Eichel, P.H.L. Notten, High Power and High Capacity 3D-Structured TiO₂ Electrodes for Lithium-Ion Microbatteries, *J. Electrochem. Soc.* 163 (2016) 2385–2389. doi:10.1149/2.1141610jes.
- [34] V. Zadin, D. Brandell, H. Kasemägi, J. Lellep, A. Aabloo, Designing the 3D-microbattery geometry using the level-set method, *J. Power Sources.* 244 (2013) 417–428. doi:10.1016/j.jpowsour.2012.12.004.

- [35] V. Zadin, H. Kasemägi, A. Aabloo, D. Brandell, Modelling electrode material utilization in the trench model 3D-microbattery by finite element analysis, *J. Power Sources*. 195 (2010) 6218–6224. doi:10.1016/j.jpowsour.2010.02.056.
- [36] M. Nathan, D. Golodnitsky, V. Yufit, E. Strauss, T. Ripenbein, I. Shechtman, et al., Three-dimensional thin-film Li-ion microbatteries for autonomous MEMS, *J. Microelectromechanical Syst.* 14 (2005) 879–885. doi:10.1109/JMEMS.2005.851860.
- [37] A.E. Fischer, K.A. Pettigrew, D.R. Rolison, R.M. Stroud, J.W. Long, Incorporation of Homogeneous, Nanoscale MnO₂ within Ultraporous Carbon Structures via Self-Limiting Electroless Deposition: Implications for Electrochemical Capacitors, *Nano Lett.* 7 (2007) 281–286.
- [38] J.W. Long, D.R. Rolison, Architectural Design, Interior Decoration, and Three-Dimensional Plumbing en Route to Multifunctional Nanoarchitectures Building the Structural Frame: Synthesis of, *Acc. Chem. Res.* 40 (2007) 854–862.
- [39] S. Ferrari, M. Loveridge, S.D. Beattie, M. Jahn, R.J. Dashwood, R. Bhagat, Latest advances in the manufacturing of 3D rechargeable lithium microbatteries, *J. Power Sources*. 286 (2015) 25–46. doi:10.1016/j.jpowsour.2015.03.133.
- [40] P. Johns, M. Roberts, J. Owen, Conformal electrodeposition of manganese dioxide onto reticulated vitreous carbon for 3D microbattery applications, *J. Mater. Chem.* 21 (2011) 10153. doi:10.1039/c0jm04357e.
- [41] M. Kotobuki, Y. Suzuki, H. Munakata, K. Kanamura, Y. Sato, K. Yamamoto, et al., Fabrication of Three-Dimensional Battery Using Ceramic Electrolyte with Honeycomb Structure by Sol–Gel Process, *J. Electrochem. Soc.* 157 (2010) A493–A498. doi:10.1149/1.3308459.
- [42] H.-S. Min, B.Y. Park, L. Taherabadi, C. Wang, Y. Yeh, R. Zaouk, et al., Fabrication and properties of a carbon/polypyrrole three-dimensional microbattery, *J. Power Sources*. 178 (2008) 795–800. doi:10.1016/j.jpowsour.2007.10.003.
- [43] G. Oltean, H. Desta Asfaw, L. Nyholm, K. Edstrom, A Li-Ion Microbattery with 3D Electrodes of Different Geometries, *ECS Electrochem. Lett.* 3 (2014) A54–A57. doi:10.1149/2.003406eel.
- [44] M. Valvo, M. Roberts, G. Oltean, B. Sun, D. Rehnlund, D. Brandell, et al., Electrochemical elaboration of electrodes and electrolytes for 3D structured batteries, *J. Mater. Chem. A*. 1 (2013) 9281–9293. doi:10.1039/c3ta11921a.
- [45] D. Rehnlund, M. Valvo, C.-W. Tai, J. Ångström, M. Sahlberg, K. Edström, et al., Electrochemical fabrication and characterization of Cu/Cu₂O multi-layered micro and nanorods in Li-ion batteries, *Nanoscale*. 7 (2015) 13591–13604. doi:10.1039/C5NR03472H.
- [46] H.D. Asfaw, M. Roberts, R. Younesi, K. Edström, Emulsion-templated bicontinuous carbon network electrodes for use in 3D microstructured batteries, *J. Mater. Chem. A*. 1 (2013) 13750–13758. doi:10.1039/c3ta12680c.
- [47] H.D. Asfaw, M.R. Roberts, C.-W. Tai, R. Younesi, M. Valvo, L. Nyholm, et al., Nanosized LiFePO₄-decorated emulsion-templated carbon foam for 3D micro batteries: a study of structure and electrochemical performance, *Nanoscale*. 6 (2014) 8804–8813. doi:10.1039/C4NR01682C.
- [48] S. Jung, D. Kang, Multi-dimensional modeling of large-scale lithium-ion batteries, *J. Power Sources*. 248 (2014) 498–509. doi:10.1016/j.jpowsour.2013.09.103.
- [49] E.B. B. Tadmor, R.E. E. Miller, *Modeling Materials*, 2011.
- [50] Z. Wang, S. Li, L. Wang, Efficient Real-Time Time-Dependent Density Functional Theory Method and its Application to a Collision of an Ion with a 2D Material, *Phys. Rev. Lett.* 063004 (2015) 1–5. doi:10.1103/PhysRevLett.114.063004.

- [51] S.S. Rao, *The Finite Element Method in Engineering*, Fifth edit, 2011. doi:10.1016/C2009-0-04807-7.
- [52] C. Grossmann, H.-G. Roos, *Numerical Treatment of Partial Differential Equations*, 2007. doi:http://dx.doi.org/10.1007/978-3-540-71584-9.
- [53] A.J. Bard, L.R. Faulkner, *Electrochemical methods: Fundamentals and Applications*, Second edi, Wiley, Austin, 2001.
- [54] R. Darling, J. Newman, Modeling a Porous Intercalation Electrode with Two Characteristic Particle Sizes, *J. Electrochem. Soc.* 144 (1997) 4201–4208. doi:10.1149/1.1838166.
- [55] M. Doyle, J. Newman, Comparison of Modeling Predictions with Experimental Data from Plastic Lithium Ion Cells, *Electrochem. Soc.* 143 (1996) 1890–1903.
- [56] M. Doyle, T.F. Fuller, J. Newman, Modeling of Galvanostatic Charge and Discharge of the Lithium / Polymer / Insertion Cell, *Electrochem. Soc.* 140 (1993) 1526–1533.
- [57] T.F. Fuller, M. Doyle, J. Newman, Simulation and Optimization of the Dual Lithium Ion Insertion Cell, *Electrochem. Sci. Technol.* 141 (1994) 1–10.
- [58] T.R. Ferguson, M.Z. Bazant, Nonequilibrium Thermodynamics of Porous Electrodes, *J. Electrochem. Soc.* 159 (2012) A1967–A1985. doi:10.1149/2.048212jes.
- [59] M. Ebner, V. Wood, Tool for Tortuosity Estimation in Lithium Ion Battery Porous Electrodes, *Electrochem. Soc.* 162 (2015) 3064–3070. doi:10.1149/2.0111502jes.
- [60] A. Nyman, M. Behm, G. Lindbergh, Electrochemical characterisation and modelling of the mass transport phenomena in LiPF₆-EC-EMC electrolyte, *Electrochim. Acta.* 53 (2008) 6356–6365. doi:10.1016/j.electacta.2008.04.023.
- [61] P. Georen, G. Lindbergh, Characterisation and modelling of the transport properties in lithium battery polymer electrolytes, *Electrochim. Acta.* 47 (2001) 577–587. doi:10.1016/S0013-4686(01)00785-X.
- [62] Q. Zhang, Q. Guo, R.E. White, Semi-empirical modeling of charge and discharge profiles for a LiCoO₂ electrode, *J. Power Sources.* 165 (2007) 427–435. doi:10.1016/j.jpowsour.2006.12.025.
- [63] F. Naznin, State of Charge (SOC) Governed Fast Charging Method for Lithium Based Batteries *, (2013) 1–7.
- [64] M. Xu, Z. Zhang, X. Wang, L. Jia, L. Yang, Two-dimensional electrochemical-thermal coupled modeling of cylindrical LiFePO₄ batteries, *J. Power Sources.* 256 (2014) 233–243. doi:10.1016/j.jpowsour.2014.01.070.
- [65] R. Liang, T. Zou, Mathematical modeling and reliability analysis of a 3D Li-ion battery, *J. Electrochem. Sci. Eng.* 4 (2014) 1–17. doi:10.5599/jese.0040.
- [66] K.A. Smith, C.D. Rahn, C.-Y. Wang, Control oriented 1D electrochemical model of lithium ion battery, *Energy Convers. Manag.* 48 (2007) 2565–2578. doi:10.1016/j.enconman.2007.03.015.
- [67] C.-W. Wang, A.M. Sastry, Mesoscale Modeling of a Li-Ion Polymer Cell, *J. Electrochem. Soc.* 154 (2007) A1035. doi:10.1149/1.2778285.
- [68] D.H. Jeon, Numerical modeling of lithium ion battery for predicting thermal behavior in a cylindrical cell, *Curr. Appl. Phys.* 14 (2014) 196–205. doi:10.1016/j.cap.2013.11.006.
- [69] K. Onda, H. Kameyama, T. Hanamoto, K. Ito, J.E. Soc, P. A-a, et al., Experimental Study on Heat Generation Behavior of Small Lithium-Ion Secondary Batteries, *Electrochem. Soc.* 150 (2003) A285–A291. doi:10.1149/1.1543947.
- [70] K. Smith, C.-Y. Wang, Power and thermal characterization of a lithium-ion battery pack for hybrid-electric vehicles, *J. Power Sources.* 160 (2006) 662–673. doi:10.1016/j.jpowsour.2006.01.038.

- [71] L. Cai, R.E. White, Mathematical modeling of a lithium ion battery with thermal effects in COMSOL Inc. Multiphysics (MP) software, *J. Power Sources*. 196 (2011) 5985–5989. doi:10.1016/j.jpowsour.2011.03.017.
- [72] M. Park, X. Zhang, M. Chung, G.B. Less, A.M. Sastry, A review of conduction phenomena in Li-ion batteries, *J. Power Sources*. 195 (2010) 7904–7929. doi:10.1016/j.jpowsour.2010.06.060.
- [73] W. Gorecki, M. Jeannin, E. Belorizky, C. Roux, M. Armand, Physical properties of solid polymer electrolyte PEO (LiTFSI) complexes, *J. Phys. Condens. Matter*. 7 (1995) 6823–6832.
- [74] D. Devaux, R. Bouchet, D. Glé, R. Denoyel, Mechanism of ion transport in PEO/LiTFSI complexes : Effect of temperature , molecular weight and end groups, *Solid State Ionics*. 227 (2012) 119–127. doi:10.1016/j.ssi.2012.09.020.
- [75] R.A. Huggins, *Advanced Batteries*, New York, 2009. doi:10.1017/CBO9781107415324.004.
- [76] E. Antolini, LiCoO₂: formation, structure, lithium and oxygen nonstoichiometry, electrochemical behaviour and transport properties, *Solid State Ionics*. 170 (2004) 159–171. doi:10.1016/j.ssi.2004.04.003.
- [77] Y. Gu, D. Chen, X. Jiao, Synthesis and Electrochemical Properties of Nanostructured LiCoO₂ Fibers as Cathode Materials for Lithium-Ion Batteries, *J. Phys. Chem. B*. 109 (2005) 17901–17906. doi:10.1021/jp0521813.
- [78] M.M. Shaijumon, E. Perre, B. Daffos, P.-L. Taberna, J.-M. Tarascon, P. Simon, Nanoarchitected 3D Cathodes for Li-Ion Microbatteries, *Adv. Mater*. 22 (2010) 4978–4981. doi:10.1002/adma.201001922.
- [79] M. Jo, S. Jeong, J. Cho, High power LiCoO₂ cathode materials with ultra energy density for Li-ion cells, *Electrochem. Commun*. 12 (2010) 992–995. doi:10.1016/j.elecom.2010.05.010.
- [80] K. Maher, R. Yazami, Effect of overcharge on entropy and enthalpy of lithium-ion batteries, *Electrochim. Acta*. 101 (2013) 71–78. doi:10.1016/j.electacta.2012.11.057.
- [81] Y.-C. Chang, C.-T. Peng, I.-M. Hung, Effects of particle size and carbon coating on electrochemical properties of LiFePO₄/C prepared by hydrothermal method, *J. Mater. Sci*. 49 (2014) 6907–6916. doi:10.1007/s10853-014-8395-9.
- [82] R. Malik, A. Abdellahi, G. Ceder, A Critical Review of the Li Insertion Mechanisms in LiFePO₄ Electrodes, *J. Electrochem. Soc*. 160 (2013) A3179–A3197. doi:10.1149/2.029305jes.
- [83] J. Molenda, A. Kulka, A. Milewska, W. Zając, K. Świerczek, Structural, Transport and Electrochemical Properties of LiFePO₄ Substituted in Lithium and Iron Sublattices (Al, Zr, W, Mn, Co and Ni), *Materials (Basel)*. 6 (2013) 1656–1687. doi:10.3390/ma6051656.
- [84] F.C. Strobridge, B. Orvananos, M. Croft, H.-C. Yu, R. Robert, H. Liu, et al., Mapping the Inhomogeneous Electrochemical Reaction Through Porous LiFePO₄ – Electrodes in a Standard Coin Cell Battery, *Chem. Mater*. 27 (2015) 2374–2386. doi:10.1021/cm504317a.
- [85] J. Liu, M. Kunz, K. Chen, N. Tamura, T. Richardson, Visualization of Charge Distribution in a Lithium-Ion Battery Electrode, *Meet. Abstr.* 02 (2010) 208.
- [86] A. Samba, N. Omar, H. Gualous, O. Capron, P. Van den Bossche, J. Van Mierlo, Impact of Tab Location on Large Format Lithium-Ion Pouch Cell Based on Fully Coupled Tree-Dimensional Electrochemical-Thermal Modeling, *Electrochim. Acta*. 147 (2014) 319–329. doi:10.1016/j.electacta.2014.08.115.

- [87] T.M. Bandhauer, S. Garimella, T.F. Fuller, A Critical Review of Thermal Issues in Lithium-Ion Batteries, *Electrochem. Soc.* 158 (2011) 1–25. doi:10.1149/1.3515880.
- [88] C. Heubner, M. Schneider, A. Michaelis, Detailed study of heat generation in porous LiCoO₂ electrodes, *J. Power Sources.* 307 (2016) 199–207. doi:10.1016/j.jpowsour.2015.12.096.
- [89] V. V. Viswanathan, D. Choi, D. Wang, W. Xu, S. Towne, R.E. Williford, et al., Effect of entropy change of lithium intercalation in cathodes and anodes on Li-ion battery thermal management, *J. Power Sources.* 195 (2010) 3720–3729. doi:10.1016/j.jpowsour.2009.11.103.
- [90] K.E. Thomas, J. Newman, Heats of mixing and of entropy in porous insertion electrodes, *J. Power Sources.* 119–121 (2003) 844–849. doi:10.1016/S0378-7753(03)00283-0.
- [91] H. Cheng, C. Zhu, B. Huang, M. Lu, Y. Yang, Synthesis and electrochemical characterization of PEO-based polymer electrolytes with room temperature ionic liquids, *Electrochim. Acta.* 52 (2007) 5789–5794. doi:10.1016/j.electacta.2007.02.062.
- [92] K. Kumaresan, G. Sikha, R.E. White, Thermal Model for a Li-Ion Cell, *J. Electrochem. Soc.* 155 (2008) 164–171. doi:10.1149/1.2817888.
- [93] J. Mao, W. Tiedemann, J. Newman, Simulation of temperature rise in Li-ion cells at very high currents, *J. Power Sources.* 271 (2014) 444–454. doi:10.1016/j.jpowsour.2014.08.033.

PUBLICATIONS

CURRICULUM VITAE

Name Priit Priimägi
Date of birth May 01, 1985
Citizenship Estonian
Address Peetri 16b–38, Tartu, 50110, Estonia
Telephone +372 5554 0646
E-mail priimagi.priit@gmail.com

Education

2014–... PhD student in the field of material science, University of Tartu. In periods, guest doctoral student at the Uppsala University, Sweden
2009–2012 University of Tartu, master studies, physics
2005–2009 University of Tartu, bachelor studies, physics

Scientific activity

Priit Priimägi, Master's degree, 2012, (sup) Heiki Kasemägi, Lithium-ion-polymer battery solid state electrolyte polyethylen/polyethylene oxide copolymer with LiPF₆ molecular dynamics simulation, University of Tartu

Languages

Estonian – native language
English – speaking good, writing good

Research

Material Science, Faculty of Science and Technology, Designing and development of 3D Li-ion microbatteries

ELULOOKIRJELDUS

Nimi Priit Priimägi
Sünniaeg 1. mai 1985
Aadress Peetri 16b–38, Tartu, 50110
Telefon +372 555 40646
e-post priimagi.priit@gmail.com

Haridus

2014–... Doktorant Tartu Ülikoolis. Perioodiliselt külalisdoktorant
Uppsala Ülikoolis, Rootsi
2009–2012 Tartu Ülikool, magistrantuur, füüsika
2005–2009 Tartu Ülikool, bakalaureuseõpe, füüsika

Teaduslik tegevus

Priit Priimägi, Magistrikraad, 2012, (juhendaja) Heiki Kasemägi, Liitiumioon-polümeeraku tahke elektrolüüdi polüetüleenipolüetüleenoksiidi kopolümeeri ja LiPF₆ molekulaardünaamiline modelleerimine, Tartu Ülikool

Keelteoskus

Eesti keel – emakeel
Inglise keel – hea

Uurimisvaldkond

Materjaliteadus, loodus ja täppisteaduste valdkond, 3D mikroakude arendamine ja optimeerimine

DISSERTATIONES SCIENTIAE MATERIALIS UNIVERSITATIS TARTUENSIS

1. **Martin Järvekülg.** Tubular microstructures by Hf-, Zr- and Ti-butoxide gel sheet rolling. Tartu, 2011, 112 p.
2. **Sergei Vlassov.** Investigation of nanoscale interactions and mechanical properties of nanostructures using quartz tuning fork based real-time measurements. Tartu, 2011, 171 p.
3. **Margus Kodu.** Pulsed Laser Deposition of Magnesium Oxide and Barium Ternary Oxides for Plasma Display Protective Layers. Tartu, 2011, 89 p.
4. **Rainer Pärna.** Surface studies of some oxide films. Tartu, 2011, 129 p.
5. **Jevgeni Šulga.** Self-assembly and interaction of nanostructures. Tartu, 2011, 114 p.
6. **Wojciech Kuznik.** Quantum-chemical computer simulations of the linear and non-linear optical properties of pyrazoloquinoline and dicyanopyrazine derivatives. Tartu, 2012, 89 p.
7. **Leonid Dorogin.** Structural and tribological properties of zero- and one-dimensional nanocrystals. Tartu, 2012, 193 p.
8. **Viljar Palmre.** Fabrication and characterization of microporous carbon-based electroactive polymer actuators. Tartu, 2012, 99 p.
9. **Madis Paalo.** Synthesis of CNT-metal oxide nanocomposites: sol-gel process, rheology, structural and functional properties. Tartu, 2014, 175 p.
10. **Raul Välbe.** Development of ionic liquid composites by sol-gel method for elaboration of industrial nano- and microstructures. Tartu, 2014, 97 p.
11. **Urmas Joost.** Impurity and preparation dependent properties of titania thin films. Tartu, 2014, 155 p.
12. **Madis Umalas.** Application of sol-gel technology for production of ceramic nanocomposites and functional coatings. Tartu, 2015, 136 p.
13. **Elena Samsonova.** Energy transfer probe as a tool to study morphological and structural origins of fluorescence quenching in rare-earth doped nanophosphors. Tartu, 2015, 114 p.
14. **Jay Mondal.** Novel Corrosion Protective Nanostructured Composite Coatings. Tartu, 2016, 104 p.
15. **Kathriin Utt.** Metal oxide mesostructures for optical applications. Tartu, 2016, 88 p.
16. **Kaido Siimon.** Electrospun gelatin cross-linked by glucose. Tartu, 2016, 84 p.
17. **Marko Part.** Combined three-dimensional sol-gel structures and atomic layer deposited thin films. Tartu, 2017, 162 p.
18. **Pejman Rasti.** Analysis of Remote Sensing Image Super Resolution using Fluid Lenses. Tartu, 2017, 188 p.
19. **Ivo Romet.** Recombination luminescence of doped borates: origin and application prospects in dosimetry. Tartu, 2017, 111 p.

20. **Vladimir I. Kondratiev.** Processing and characterization of transparent electrode materials. Tartu, 2017, 111 p.
21. **Taivo Jõgiaas.** Mechanical properties of atomic layer deposited thin films and nanocomposites. Tartu, 2017, 125 p.
22. **Lauri Aarik.** Atomic layer deposition and characterization of thin oxide films for application in protective coatings. Tartu, 2017, 180 p.
23. **Triin Kangur.** Preparation and functional properties of stochastic microstructured sol-gel silica materials. Tartu, 2018, 96 p.
24. **Marta Berholts.** Fragmentation of ionic and hydrogen-bonded molecules induced by synchrotron radiation. Tartu, 2018, 126 p.